

Coseismic and postseismic slip associated with the 2010 Maule Earthquake, Chile: Characterizing the Arauco Peninsula barrier effect

Yu-nung Nina Lin,¹ Anthony Sladen,² Francisco Ortega-Culaciati,¹ Mark Simons,¹ Jean-Philippe Avouac,¹ Eric J. Fielding,³ Benjamin A. Brooks,⁴ Michael Bevis,⁵ Jeff Genrich,¹ Andreas Rietbrock,⁶ Christophe Vigny,⁷ Robert Smalley,⁸ and Anne Socquet⁹

Received 17 October 2012; revised 4 March 2013; accepted 1 May 2013.

[1] Observations of coseismic and postseismic deformation associated with the 2010 $M_w = 8.8$ Maule earthquake in south-central Chile provide constraints on the spatial heterogeneities of frictional properties on a major subduction megathrust and how they have influenced the seismic rupture and postseismic effects. We find that the bulk of coseismic slip occurs within a single elongated patch approximately 460 km long and 100 km wide between the depths of 15 and 40 km. We infer three major patches of afterslip: one extends northward along strike and downdip of the major coseismic patch between 40 and 60 km depth; the other two bound the northern and southern ends of the coseismic patch. The southern patch offshore of the Arauco Peninsula is the only place showing resolvable afterslip shallower than 20 km depth. Estimated slip potency associated with postseismic slip in the 1.3 years following the earthquake amounts to 20–30% of that generated coseismically. Our estimates of the megathrust frictional properties show that the Arauco Peninsula area has positive but relatively low $(a-b)\sigma_n$ values (0.01 ~ 0.22 MPa), that would have allowed dynamic rupture propagation into this rate-strengthening area and afterslip. Given the only modestly rate-strengthening megathrust friction in this region, the barrier effect may be attributed to its relatively large size of the rate-strengthening patch. Coseismic and postseismic uplift of the Arauco Peninsula exceeds interseismic subsidence since the time of the last major earthquake in 1835, suggesting that coseismic and postseismic deformation has resulted in some permanent strain in the forearc.

Citation: Lin, Y.-n. N., et al. (2013), Coseismic and postseismic slip associated with the 2010 Maule Earthquake, Chile: Characterizing the Arauco Peninsula barrier effect, *J. Geophys. Res. Solid Earth*, 118, doi:10.1002/jgrb.50207.

1. Introduction

[2] Large megathrust earthquakes frequently trigger aseismic frictional afterslip on the megathrust in regions that are complementary to those that slipped coseismically [e.g., *Miyazaki*

et al., 2004; *Ozawa et al.*, 2004; *Baba et al.*, 2006; *Hsu et al.*, 2006; *Pritchard and Simons*, 2006; *Perfettini et al.*, 2010; *Vigny et al.*, 2011; *Ozawa et al.*, 2012]. The amplitude of afterslip is generally estimated to range from tens of centimeters to several meters (partially dependent on the size of the mainshock, the time span of the observations, and the approach used to infer afterslip), and the location can range from near the trench to as deep as 100 km. Aftershocks tend to cluster along the boundary between the coseismic and postseismic slip zones [e.g., *Hsu et al.*, 2006; *Agurto et al.*, 2012; *Ozawa et al.*, 2012]. The observed spatial and temporal correlation between afterslip and aftershocks, and the small contribution of the latter to the total postseismic energy release, suggest that aftershocks are at least partly triggered by afterslip [*Perfettini and Avouac*, 2004; *Hsu et al.*, 2006; *Pritchard and Simons*, 2006; *Perfettini et al.*, 2010]. All these observations suggest that megathrust frictional properties are heterogeneous, allowing interfingering and interplay of seismic and aseismic slip from the trench all the way down to 100 km. However, it is generally difficult to really assess true differences in fault properties due to heterogeneity in models resolution.

Additional supporting information may be found in the online version of this article.

¹California Institute of Technology, Pasadena, California, USA.

²Géoazur, Université de Nice Sophia-Antipolis, CNRS, Observatoire de la Côte d'Azur, Valbonne, France.

³Jet Propulsion Laboratory, La Cañada, California, USA.

⁴University of Hawaii, Honolulu, Hawaii, USA.

⁵Ohio State University, Columbus, Ohio, USA.

⁶University of Liverpool, Liverpool, UK.

⁷École Normale Supérieure, Paris, France.

⁸University of Memphis, Memphis, Tennessee, USA.

⁹Université Joseph Fourier, Grenoble, France.

Corresponding author: Y.-n. N. Lin, California Institute of Technology, C100-23, 1200 E California Blvd., Pasadena, CA 91125, USA. (ninalin@gps.caltech.edu)

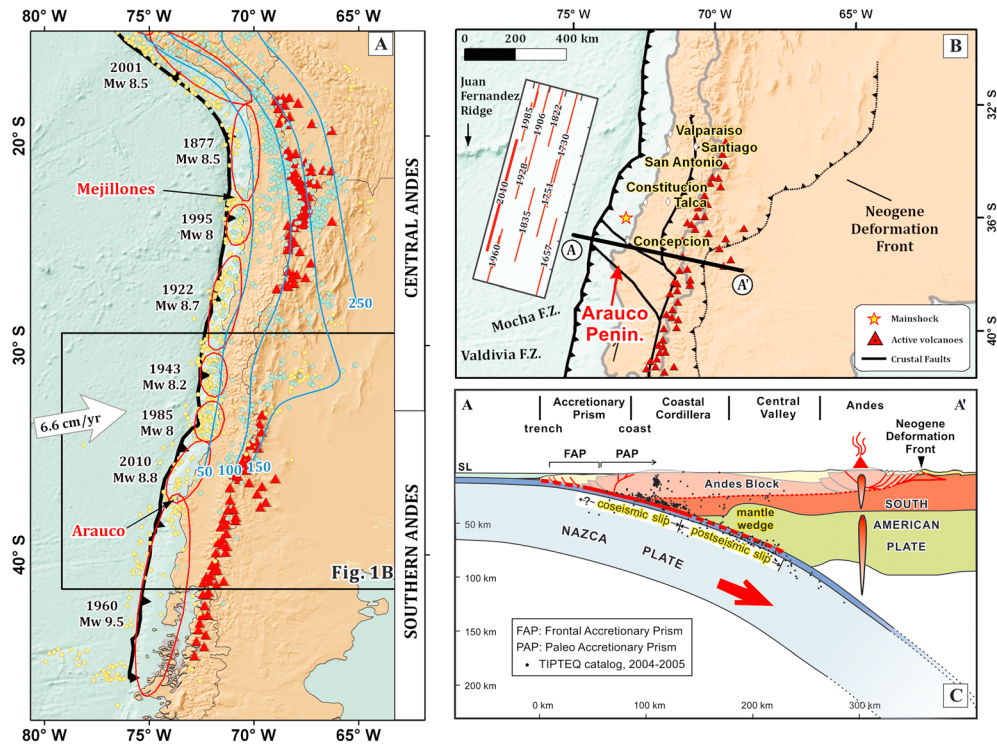


Figure 1. (a) Regional tectonic map showing slab isodepth contours (blue lines) [Cahill and Isacks, 1992], $M \geq 4$ earthquakes from the National Earthquake Information Center catalog between 1976 and 2011 (yellow circles for depths less than 50 km, and blue circles for depths greater than 50 km), active volcanoes (red triangles), and the approximate extent of large megathrust earthquakes during the past hundred years (red ellipses) modified from Campos *et al.* [2002]. The large white vector represents the direction of Nazca Plate with respect to stable South America [Kendrick *et al.*, 2003]. (b) Simplified seismo-tectonic map of the study area. Major Quaternary faults are modified after Melnick *et al.* [2009] (black lines). The Neogene Deformation Front is modified from Folguera *et al.* [2004]. The west-vergent thrust fault that bounds the west of the Andes between 32° and 38° S is modified from Melnick *et al.* [2009]. (c) Schematic cross-section along line A–A' (Figure 1b), modified from Folguera and Ramos [2009]. The upper bound of the coseismic slip coincides with the boundary between the frontal accretionary prism and the paleo-accretionary prism [Contreras-Reyes *et al.*, 2010], whereas the contact between the coseismic and postseismic patch is from this study. The thick solid red line and dashed red line on top of the slab represent the approximate coseismic and postseismic plus interseismic slip section of the subduction interface. The thin red and grey lines within the overriding plate are active and inactive structures in the retroarc, modified from Folguera and Ramos [2009]. The red dashed line underneath the Andean Block represents the regional décollement. Background seismicity is from the TIPTEQ catalog, recorded between November 2004 and October 2005 [Rietbrock *et al.*, 2005; Haberland *et al.*, 2009].

[3] In this study, we estimate the distribution of coseismic and postseismic slip to assess the spatial variability of frictional properties on the south-central Chilean megathrust. As inferred from the strong correlation between coseismic slip patches and large-amplitude gravity anomalies in the region of a majority of (but not all) recent large earthquakes [Song and Simons, 2003], the along-strike variations in frictional behavior appear to persist over multiple earthquake cycles [Song and Simons, 2003; Wells *et al.*, 2003; Loveless *et al.*, 2010]. Several long-lived geologic features are also correlated with differences in slip behavior on the megathrust. For example, the most prominent patch of aseismic fault slip after the Pisco earthquake in central Peru coincides with the subducting Nazca ridge, which seems to have repeatedly acted as a barrier to seismic rupture propagation in the past [Perfettini *et al.*, 2010]. The region of peak afterslip after the Antofagasta earthquake lies immediately beneath the

Mejillones Peninsula, a proposed segment boundary during multiple seismic events, whose Quaternary deformation history is consistent with postseismic uplift [Pritchard and Simons, 2006; Béjar-Pizarro *et al.*, 2010; Victor *et al.*, 2011]. Along the Sumatran megathrust, the segment boundary beneath the Batu Islands also correlates with the subduction of the Investigator Fracture Zone [Chlieh *et al.*, 2008].

[4] South-central Chile is an ideal natural laboratory to study the different stages of the seismic cycle and the role of purported seismic barriers because of the information available on past seismic ruptures, strain accumulation in the interseismic period, and the seismological and geodetic constraints on the recent Maule earthquake [Ruegg *et al.*, 2002; Moreno *et al.*, 2008; Ruegg *et al.*, 2009; Moreno *et al.*, 2010; Delouis *et al.*, 2010; Lay *et al.*, 2010; Vigny *et al.*, 2011; Lorito *et al.*, 2011]. The Arauco Peninsula is of particular interest because it coincides with the boundary

between the $M_w=8.8$ 2010 Maule and the $M_w=9.5$ 1960 Valdivia earthquakes (Figure 1a), and in particular may be the location of the 1960 Valdivia earthquake's $M_w=8.1$ foreshock that was located very close to Concepción [Cifuentes, 1989]. Thus, the region of the megathrust below the Arauco Peninsula area has acted as a seismic barrier over at least a few hundred years [Barrientos and Ward, 1990; Moreno et al., 2009; Delouis et al., 2010; Lay et al., 2010]. Melnick et al. [2009] showed that the peninsula is a zone of rapidly accumulating geological deformation and further proposed that the Arauco acts as a permanent barrier to propagating seismic ruptures on the million-year time scale. They suggest that the Arauco barrier results from the juxtaposition of heterogeneous metamorphic rocks with homogeneous intrusive rocks (Figure 1b), causing a compositional and hence mechanical discontinuity in the crust all the way down to the plate interface. A possible alternative is that the Arauco Peninsula would overlie a section of the megathrust that is dominantly aseismic. Zones of aseismic creep have been proposed to act as permanent barriers based on numerical simulations [Kaneko et al., 2010] and observations [e.g., Chlieh et al., 2008; Konca et al., 2008]. To explore this issue, we infer the distribution of coseismic and postseismic slip associated with the 2010 Maule earthquake and estimate the frictional properties along the megathrust.

[5] To assess the uncertainties and resolution in different slip models, we first derive our own coseismic slip model by using an expanded set of available GPS, InSAR (Interferometric Synthetic Aperture Radar), teleseismic, and tsunami data. We then derive a postseismic slip model relying on GPS and InSAR observations. We integrate these slip models with the distribution of aftershocks to further illuminate the seismic/aseismic behavior of the megathrust. Finally, we discuss the implications of these slip patterns in terms of associated potency or equivalent moment and implications for the frictional behavior of the megathrust.

2. The 2010 Maule Earthquake and Its Seismotectonic Settings

[6] Prior to 2010, the Concepción-Constitución region experienced three large historical megathrust earthquakes in 1730, 1751, and 1835 (Figure 1b) [Campos et al., 2002; Lomnitz, 2004]. Among these large historic events, the 1730 $M=8.5\sim 9$ Great Valparaíso earthquake generated a sizable tsunami [Lomnitz, 2004]. The 1751 $M=8.5$ Concepción earthquake generated an even larger and more destructive tsunami. The last large earthquake, with an estimated magnitude of 8.5, has been described by Charles Darwin during the voyage of the HMS *Beagle* in 1835 [Darwin, 1851]. He and captain FitzRoy reported numerous geological phenomena that accompanied the earthquake, including coseismic coastal uplift/subsidence, postseismic deformation, tsunami waves of intermediate amplitude, and volcanic activity. Later in 1928, a smaller event, the $M=7.9$ Talca earthquake devastated the towns of Talca and Constitución and produced a local tsunami height of only 1.5 m [Beck et al. 1998]. During the 1960 Valdivia earthquake, the $M_w=8.1$ foreshock ruptured only the southernmost part of this segment [Cifuentes, 1989]. Thus, for the majority of the Concepción-Constitución segment, there had been no major subduction earthquakes since 1835 [Beck et al., 1998; Campos et al., 2002]. The potential

for a $M_w=8\sim 8.5$ earthquake in this region, based on the seismic gap hypothesis, was recognized before the 2010 event [Ruegg et al., 2009], although Lorito et al. [2011] argued that the overall slip distribution of the 2010 event is inconsistent with that expected from the seismic gap hypothesis [Campos et al., 2002; Ruegg et al., 2002; Moreno et al., 2008; Ruegg et al., 2009; Madariaga et al., 2010; Moreno et al., 2010].

[7] The 1960 $M=9.5$ South Chile earthquake occurred to the south of the Concepción-Constitución segment in a region referred to as the Valdivia segment [Cifuentes, 1989; Barrientos and Ward, 1990] (Figure 1a). This earthquake was preceded historically by earthquakes in 1575, 1737, and 1837 [Lomnitz, 2004]. The 1575 and 1837 earthquakes produced only small tsunamis at the Rio Maullín estuary in the center of the 1960 rupture and they are now believed to be considerably smaller than the 1960 event [Lomnitz, 2004; Cisternas et al., 2005] (Figure 1a). Between this segment and the Concepción-Constitución segment lies the Arauco Peninsula, a major anomaly along the Pacific margin of South America in terms of coastline morphology and trench-to-coast distance (Figure 1a).

[8] The 2010 Maule earthquake nucleated northwest of Concepción [Delouis et al., 2010; Lay et al., 2010], with an epicenter located at 36.41°S and 73.18°W as determined using high-rate GPS records [Vigny et al., 2011]. The rupture appears to have propagated bilaterally through two major asperities and caused severe damage to the city of Constitución, Santiago, Talca, and various others (Figure 1b) [Astroza et al., 2010]. The hinge line between surface uplift and subsidence generally lies along the coastline. The only exception is the Arauco Peninsula, where the hinge line cuts through the east of the peninsula and where coastal uplift of up to 240 ± 20 cm was observed [Vargas et al., 2011]. This observation alone points to the peculiar nature of the Arauco Peninsula. Tsunami waves affected the coastal regions between the cities of Valparaíso and Valdivia, with a peak runup of 29 m on a coastal bluff at Constitución. In most places runup heights are less than 10 meters [Fritz et al., 2011].

[9] Currently there are at least six different published coseismic slip models (see supplementary materials of Vigny et al. [2011]; also see Moreno et al. [2012]). Major differences between these models include: (1) the updip extent of the primary slip zone (defined by 5 m slip contour), which may extend to the trench (modeling with teleseismic data only, e.g., Lay et al. [2010]), stop at 5–10 km (modeling with geodetic data only, e.g., Tong et al. [2010]; Vigny et al. [2011]; Moreno et al. [2012]), or even stop 10–20 km downdip from the trench [e.g., Delouis et al., 2010; Lorito et al., 2011]; (2) the center of the southern slip patch may be to the north of the Arauco Peninsula [Delouis et al., 2010; Lay et al., 2010], right under the peninsula [Tong et al., 2010; Lorito et al., 2011; Moreno et al., 2012], or to the west of the peninsula [Vigny et al., 2011]. These published models of fault slip adopt different forms of regularization and boundary conditions and also consider different data sets, thereby making it difficult to compare models. In this study, we develop our own coseismic slip model. By doing so, we can better understand the resolution limit, the contribution and consistency of different data sets, the impact of regularization terms, and the extent to which we can use these models to extract reliable information on fault zone behavior. More importantly, we ensure that our coseismic

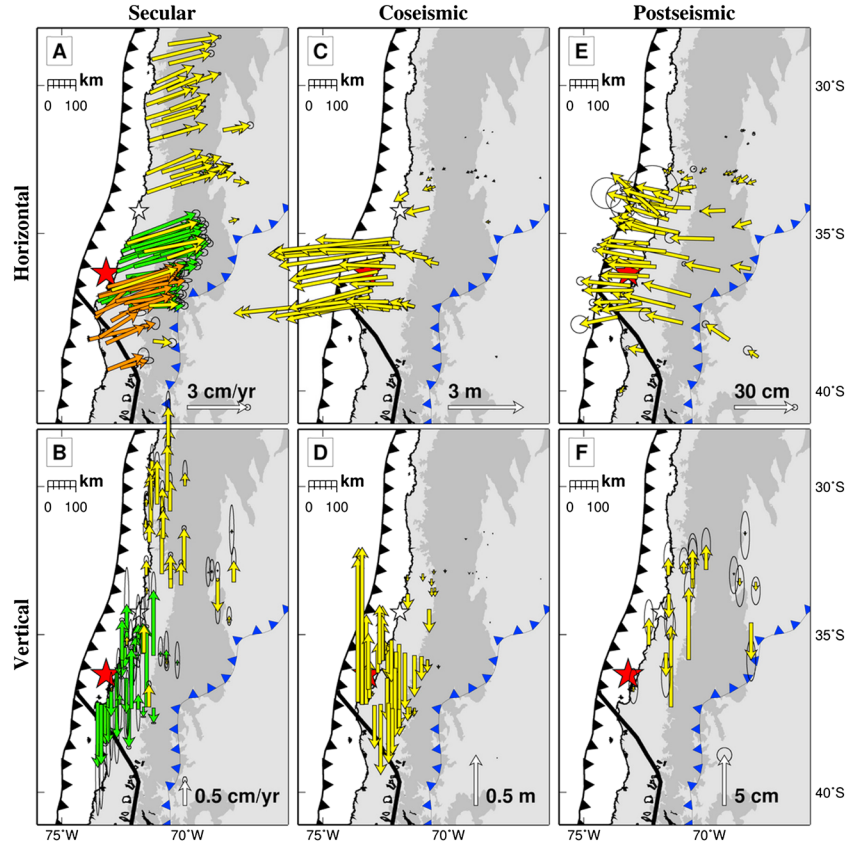


Figure 2. Horizontal and vertical secular interseismic velocities (left), coseismic displacement (middle) and postseismic displacement spanning the period between the 1st and 488th day after the mainshock (right). Note that for the postseismic displacement, when actual data time span for a given record does not cover this whole period, we have extrapolated it to represent the deformation between the 1st and 488th day using principal component analysis-based inversion method. Yellow vectors are derived from this study; green vectors and orange vectors in Figures 2a and 2b are from *Ruegg et al.* [2009] and *Moreno et al.* [2008], respectively. The blue barbed line corresponds to the Neogene Deformation Front. The red and white stars represent the epicenter of the mainshock and the Pichilemu earthquake, respectively. The dark grey region is bounded by the 1000 m contour line, approximately the boundary of the Andes.

and postseismic models are affected by the same potential bias introduced by the inversion procedure and the simplifications made to compute the Green's functions.

3. Data

[10] We combined GPS data from multiple networks (see Table S1 in the supporting information), resulting in a total of 127 three-component continuous records. We use a conventional least-squares approach to separate postseismic deformation from other signals, including secular rates, coseismic jumps (e.g., the Maule main shock, Pichilemu aftershock, and other events), and seasonal variations (Figure 2). For the short time series whose records start after the Maule earthquake, we determined their horizontal secular rates and seasonal variations by using velocities from the long time series and from published literature (Figure 2a) [*Moreno et al.*, 2008; *Ruegg et al.*, 2009]. We did not carry out the same corrections on the vertical components due to the large uncertainties in their secular rates (Figure 2b) [*Ruegg et al.*, 2009], but chose to use only the long time series in our postseismic model. In the end, 79 three-component coseismic

displacements are determined with 27 of them, mostly far-field stations, augmenting the data set described in *Vigny et al.* [2011]; 66 cGPS stations are used in the postseismic model, among which 22 vertical records were considered usable.

[11] By inspecting the cumulative postseismic displacements (Figures 2e and 2f) we found the peak horizontal displacement near the coast as expected; however, the peak vertical displacement occurs near the Andes. This pattern is different from any analytical prediction of a thrust fault system in an elastic half-space or layered half-space (Figures 2c and 2d). The peculiarity in the postseismic data therefore indicates such models will have difficulty in fitting all the postseismic data with simple models of slip restricted to the megathrust.

[12] Besides GPS time series, the Japanese L-band Advanced Land Observation Satellite (ALOS) provided continuous monitoring along this region after the earthquake for almost one year (Figure 3). Among the data ALOS acquired, wide-swath descending track 422 forms the most continuous image of the coseismic and early postseismic deformation field (Figures 3 and 4). In addition to this wide-swath track, ascending tracks 111 through 119 provide continuous spatial coverage over different time spans all the way through the end of 2010.

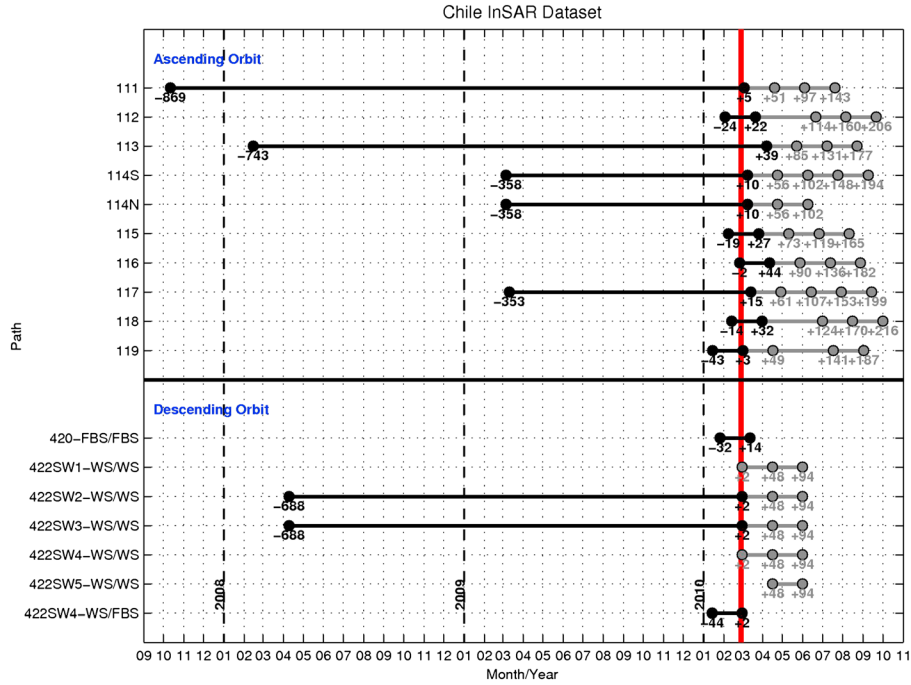


Figure 3. ALOS PALSAR acquisitions used in this study. FBS stands for fine mode single polarization mode while WS stands for wide swath data. Black lines indicate coseismic pairs and gray lines indicate postseismic pairs. Numbers under each acquisition dot represent the number of days before or after the earthquake.

We refer the reader to the supporting information for more details regarding the GPS data processing, corrections applied to coseismic and postseismic InSAR images and the issues associated with data sampling.

4. Coseismic Slip Model

[13] To solve for the distribution of coseismic slip of the Maule earthquake, we perform a joint inversion of all the static data previously described (i.e., InSAR and GPS) and teleseismic body waves (Figure 5; also see supporting information for model details) using the method of *Ji et al.* [2002]. Consistent with previous models, our preferred coseismic slip model indicates that rupture was bilateral and extended over 500 km (Figure 5c). The slip model defines a relatively continuous band of significant slip extending ~ 100 km down dip that parallels but extends only slightly below the coastline (Figure 6). The distribution of slip is dominated by a region of high slip north of the epicenter (centered around latitude $S35^\circ$) with a maximum slip of 16 m, close to the 15 m peak slip from *Vigny et al.* [2011]. In the southern part of the rupture, near the Arauco Peninsula, the slip distribution is more irregular with slip amplitudes not exceeding 8 m.

[14] The coseismic model allows us to reproduce the main characteristics of the different data sets (Figures 4–6). There are several residual fringes in some of the InSAR tracks. However, given the orientation of those residual fringes, we suspect unmodeled propagation delays due to ionospheric perturbations or nonoptimal orbital ramp corrections. In the case of the GPS data, all vectors are fit extremely well with the exception of the vertical component of the profile extending eastward from Constitución around latitude $S35.3^\circ$. In essence, the region of observed coseismic

subsidence is narrower (i.e., with a more limited eastward extent) than what our model produces (Figure 6). Extending the downdip limit of our fault geometry allows improvement in the fit to the vertical displacements by allowing localized slip patches beneath the problematic stations near the Andes. Given the correlation of these deep slip patches with the sparse location of the GPS stations, we are not sure if they are reliable or if they reflect, for instance, an oversimplification in the model fault geometry and elastic model. We note that *Moreno et al.* [2012] adopted a finite-element model that takes more subtleties in the fault geometry into account, but their results also show the same residuals in the GPS vertical components near the Andes. We return to this point later in the discussion section.

[15] To limit the potential trade-off between rupture time and rupture duration, which is enhanced by the bilateral rupture [e.g., *Lay et al.*, 2010], and to limit the nonuniqueness of the solution, we impose a narrow prior range of $2.5\text{--}3.0\text{ km}\cdot\text{s}^{-1}$ for the rupture velocity [*Delouis et al.*, 2010; *Vigny et al.*, 2011] and allow each patch to rupture only once for a maximum of 14 s. Despite these strong prior constraints on the solution, we obtain a slip distribution similar to the geodetic-only inversion (Figure S3) with a reasonable fit of the complex teleseismic *P* wave train (Figure 5).

[16] Coseismic slip in our preferred model stops about 15 km from the trench at the latitude of maximum slip (Figure 5). This behavior is similar to the models of *Delouis et al.* [2010] and *Lorito et al.* [2011], who also included multiple data types in their inversions. This slip extent agrees well with the 90% coupling patch determined by the interseismic GPS measurements during the past decade [*Métois et al.*, 2012], although the resolution of the near-trench portion of the megathrust is significantly

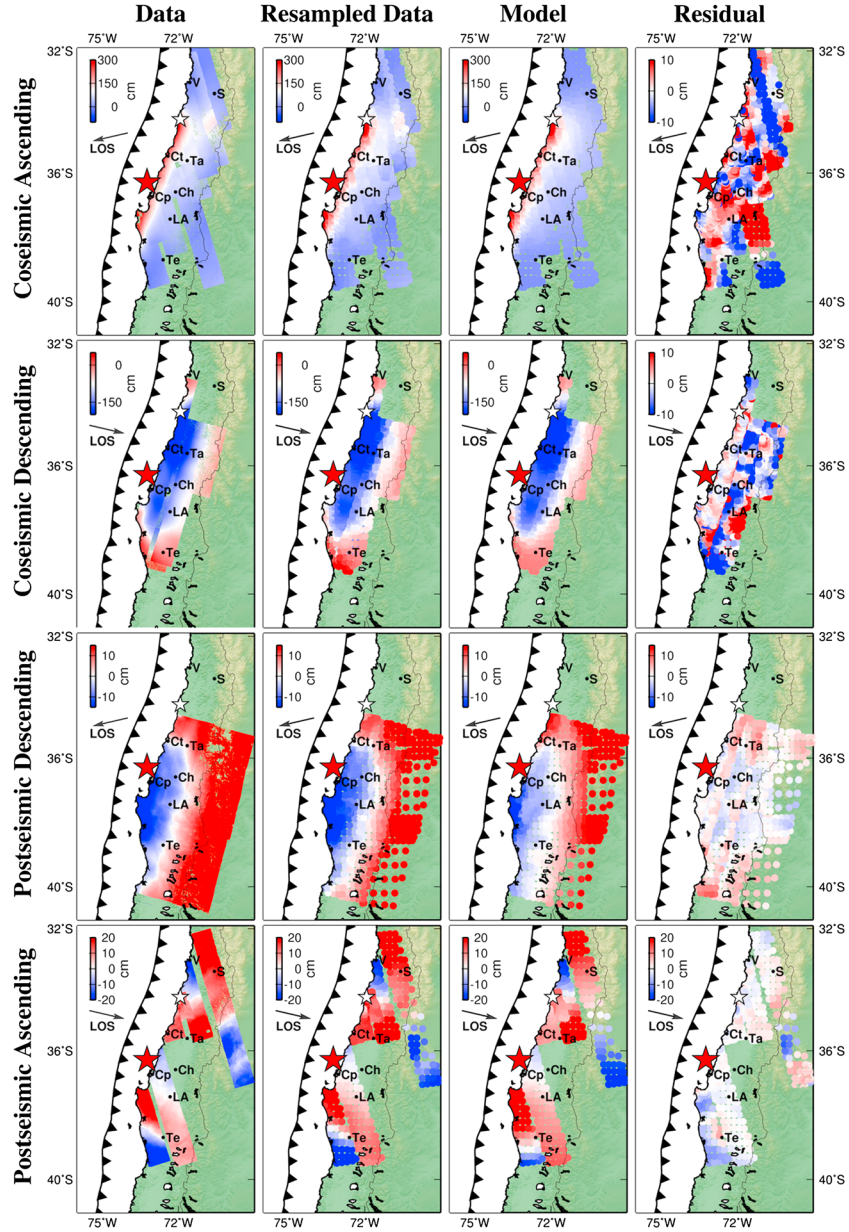


Figure 4. The original, resampled, modeled InSAR data, and the model residuals for both the coseismic and postseismic tracks. Red and white stars are for the Maule and Pichilemu earthquakes, respectively. Notice that for the postseismic ascending images, different tracks cover different time spans (Figure 3) and therefore they cannot form a continuous map as the postseismic descending tracks.

reduced. Coseismic slip on the shallowest part of the megathrust is difficult to constrain from on-land geodetic data alone because of the decreases in resolution with distance from the observations (illustrated by a checkerboard test in Figure S4). In addition to this well-established limitation, resolution is also affected by model errors, that is, the use of approximate Green's functions, not taking into account complex fault geometry (e.g., splay-faults), the effect of topography, and of gradients in material properties [e.g., Hsu et al., 2011]. To illustrate just one of these effects, we estimated a solution adopting a homogeneous elastic half-space instead of a 1-D layered half-space. The result (Figure S8) shows a slip distribution very similar to our preferred model but with slip extending closer to the trench. This simple test

illustrates that the extent of shallow slip may be fairly sensitive to the assumed velocity structure. This conclusion is also supported by the checkerboard and sensitivity tests performed on the coseismic and postseismic models (Figures S4, S6, and S7).

[17] On the other hand, tsunami data recorded in the open ocean is sensitive to the outer extent of the megathrust rupture and can be used to constrain the rupture of large subduction earthquakes [e.g., Satake, 1993; Piatanesi and Lorito, 2007; Sladen and Hébert, 2008; Sladen et al., 2010; Lorito et al., 2011; Simons et al., 2011]. The tsunami simulation for our slip model, using the tsunami model described in Heinrich et al., [1998] and Hébert et al. [2001], provides good predictions of the tsunami waveforms at nearby tide

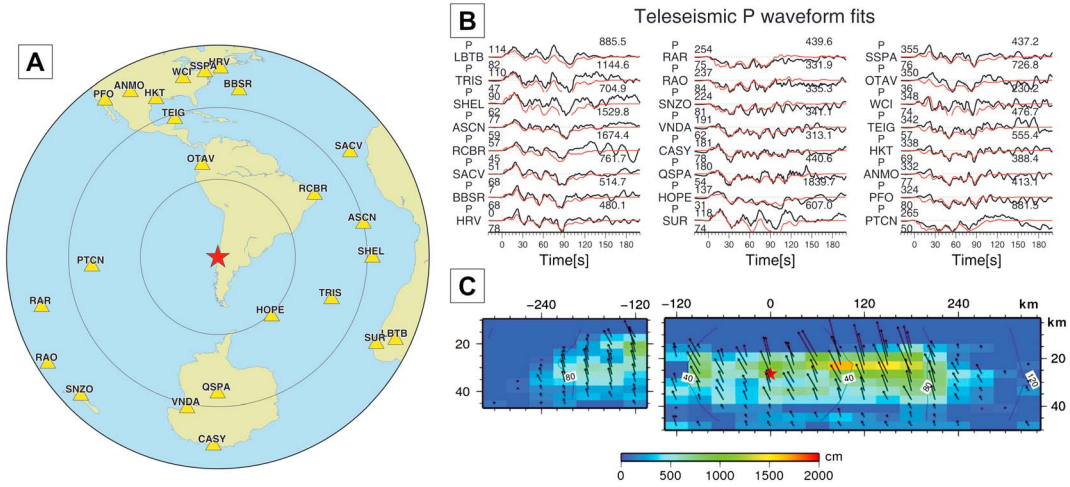


Figure 5. (a) The global distribution of seismic stations used in the coseismic model. Circles are every 30° of azimuthal distance. (b) Comparison of the observed (black) and modeled seismic waveforms (red) of the kinematic finite fault model. (c) The slip magnitude (colors), rake (arrows) and rupture propagation time in seconds (isochrones) for that same kinematic model.

gauges (with the exception of the Ancud and Corral tide gages located deep inside complex bays) and open-ocean buoys, but arrives too early at most stations south of the main tsunami energy beam (Figure 7). Back-projection of the tsunami (Figure S9) indicates that only buoy 51406 is directly sensitive to the slip distribution updip of the main slip patch (see supporting information). Even considering the effects of

rupture propagation, the tsunami simulation of our preferred slip model arrives 4 min too early at that 51406 station (Figure 7), suggesting that it is unlikely that the slip extended even closer to the trench. This argument is consistent with the study of *Lorito et al.* [2011] who included the tsunami records in their inversion of the slip distribution. However, this result mainly relies on one distant station and we cannot

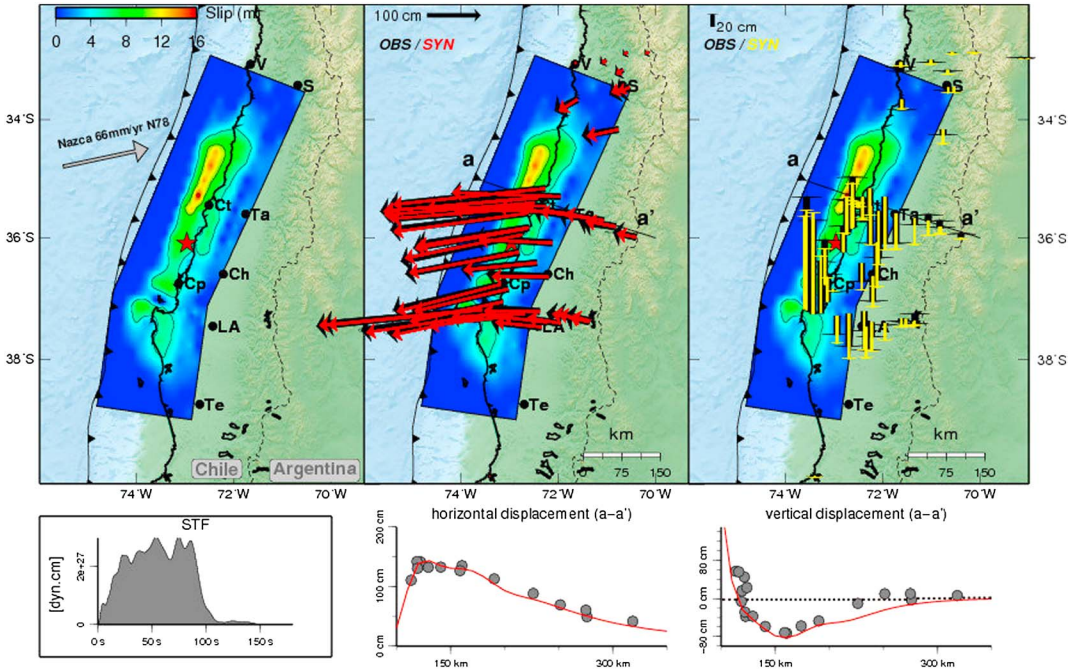


Figure 6. (left) Coseismic slip with 5 m contour intervals from the best-fit model with the source time function of the solution plotted below. (center and right) Black vectors indicate the observed GPS data; red and yellow vectors indicate modeled results in the horizontal and vertical components, respectively. The profile (aa') shows the predicted (red line) and observed (grey solid dots) surface displacements at the latitude of the main asperity, around latitude 36° S. Notice that for the vertical components (right), the slip model predicts a displacement field of longer wavelength than the observed data. See text for a discussion of this discrepancy. STF: Source time function. Ch: Chillán; Ct: Constitución; Cp: Concepción; LA: Los Angeles; Ta: Talca; Te: Temuco; S: Santiago; V: Valparaiso.

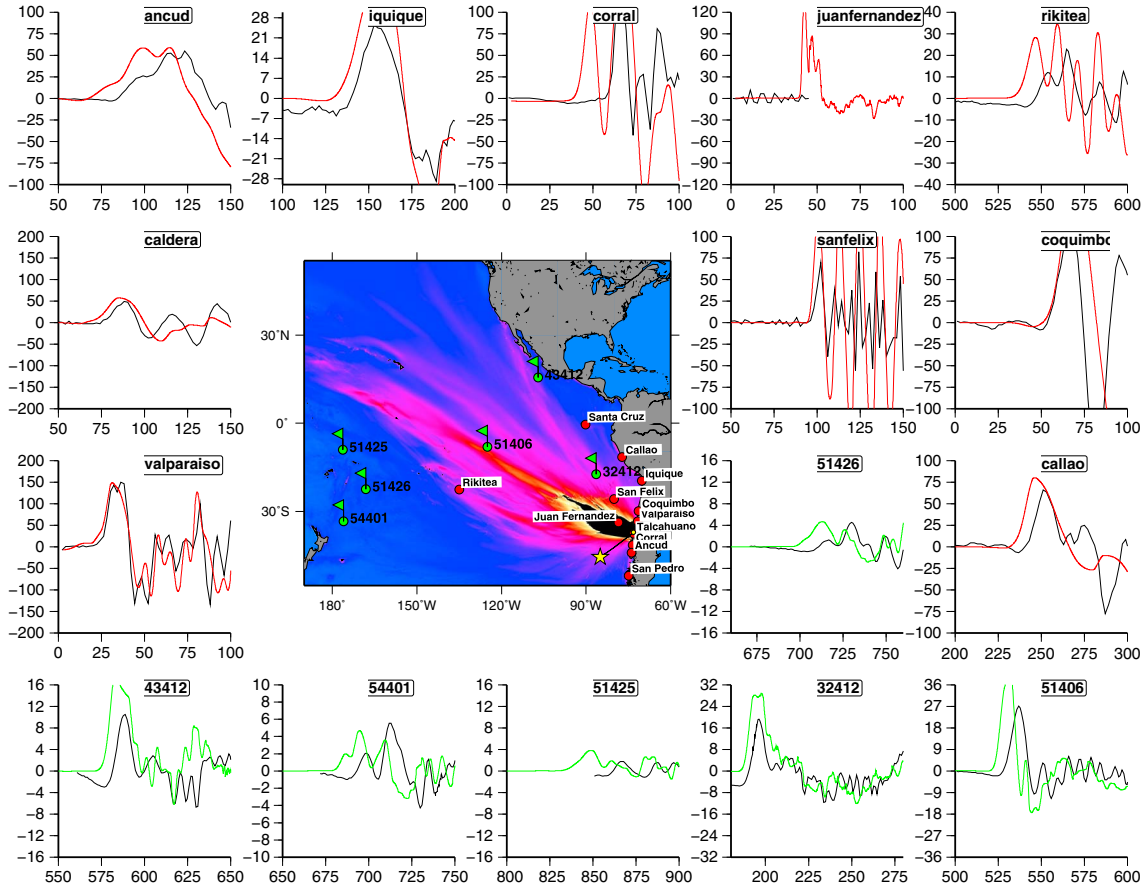


Figure 7. Tsunami records as predicted by our preferred kinematic source model—these data were not used in the construction of the model. Black lines are observations; red and green lines are the modeled waves for tide gauges and deep-sea bottom pressure gauges, respectively. The map in the middle shows the predicted maximum open ocean wave heights. No time shift has been applied to the records.

exclude the possibility that dispersion effects not taken into account in the shallow-water approximation could have biased the timing of that tsunami record.

[18] The along-strike extent of our preferred slip model, as defined by areas with slip in excess of 5 m, is about 460 km. The northern edge of the slip model (at latitude 34°S) is remarkably sharp, a characteristic also visible in the source time function which abruptly stops after 100 s. This sharp rupture termination may have promoted the static triggering of the Pichilemu aftershock sequence [Farias *et al.*, 2010; Vigny *et al.*, 2011]. The southern slip patch is centered under the Arauco Peninsula, extending slightly northwestward. This pattern agrees with several published results in general [Tong *et al.*, 2010; Lorito *et al.*, 2011; Moreno *et al.*, 2012]. The total seismic moment of our slip model is $2.25e+21$ N·m, equivalent to M_w 8.8, a value close to that estimated by GCMT ($1.86e+21$ N·m).

5. Postseismic Slip Model

[19] There are a few differences in the construction of the coseismic and postseismic slip models. To derive the time-dependent finite source kinematic models, we use the principal component analysis-based inversion method [Kositsky and Avouac, 2010; Lin *et al.*, 2010]. We build a larger fault plane

because postseismic slip may take place at greater depth. The fault plane for the postseismic model assumes a curved shape to fit the geometry imaged by various techniques (seismicity, tomography, and so on). In addition, we apply the sensitivity-modulated regularization scheme from the work of Ortega-Culaciati *et al.* (in preparation, 2013) to take care of the model resolution at different depths. The details of these changes are described in the supporting information.

[20] The RMS residual is 0.9 cm for the horizontal GPS observations and 1.1 cm for vertical components. These values reflect both measurement and prediction error. We find systematic residuals for the GPS observations near the Andes, including SJAV, CURI, MAUL, and ELA2 in the north and UDEC, ANTC, LAJA, LMNS, and ESQA in the south (Figure 8). The E-W components of the time series of these stations display a slower westward increase during the initial postseismic period when compared with other stations, but a faster trend after the first 200 days. The misfit to these stations suggests a modeling inadequacy in our layered elastic half-space afterslip model. We discuss these misfits further in section 6.4

[21] In Figure 9 we compare three postseismic slip models, constrained by GPS horizontal components only, GPS horizontal plus vertical components, and three-component GPS plus InSAR data sets, respectively. Strike-slip motion in

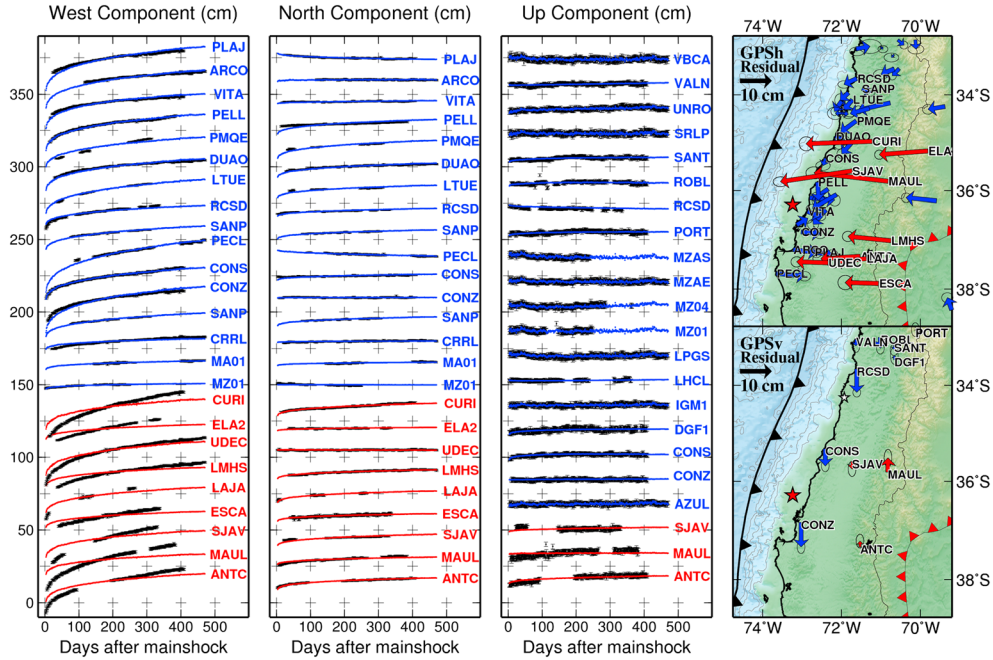


Figure 8. Time series of selected GPS stations. Blue lines and stations represent predicted time series that agree well with the data (black dots), whereas red lines and stations represent model prediction displaying large discrepancies with the data. The map views at the right panel show the residual vectors between the observed and modeled GPS components. The red stations are distributed along the Andes, indicating that the large systematic residuals are likely due to a common source.

these models is minor, so we can treat the slip as primarily dip-slip motion. The comparison of the patterns between the first two models (Figures 9a and 9b) reveals nuances, particularly the connectivity, in the afterslip patch downdip of the coseismic slip region. This elongated zone, designated as **A**, extends from almost 40 to 60 km at depth, with maximum slip of ~ 1.8 m over the first 488 days after the mainshock. This creeping zone generally agrees with the results from *Vigny et al.* [2011] but is more spatially focused, due to a combination of the augmented GPS and InSAR data and the differing forms of regularization employed. This elongated afterslip zone also coincides with the downdip slip deficit zone proposed by *Moreno et al.* [2012].

[22] Incorporating the InSAR data set (Figure 9c) allows us to resolve a shallow afterslip patch offshore of the Arauco Peninsula and a deep slip patch that is separated from the main slip patch. The offshore region of slip, designated as **B**, is the only region with slip shallower than 20 km. Slip on this patch is constrained primarily by InSAR observations, as we only have one near-coast GPS station between latitudes 38° and 40° S. This lack of GPS data is why this region of afterslip was not captured in the early model of *Vigny et al.* [2011]. A third slip patch that is not as shallow as patch **B** is located to the northern edge of the coseismic slip patch. This patch, designated as **C**, is between 20 and 40 km at depth. Its spatial extent agrees well with the results from *Vigny et al.* [2011]. Patch **B** and **C** together bound the southern and northern edge of the whole coseismic slip patch and agree with the Arauco and San Antonio intersegment area that define the Maule segment in *Métois et al.* [2012].

[23] The deep slip patch, designated as **D**, extends to 120–160 km at depth. This region of slip is spatially distinct from patch **A** and **B** located further updip. The slip on this patch is also primarily constrained by InSAR, because the residuals for the GPS observations in this region are large. It is therefore likely that our model maps some uncorrected noise in InSAR data (atmospheric noises in particular because this patch is close to the Andes) or other geophysical processes in the InSAR data onto the subduction interface. Given these issues, we do not interpret the slip in this patch further.

[24] Except for patch **B**, we do not see significant afterslip updip of the regions that slipped coseismically, i.e., from the trench to 20 km at depth. This result agrees with the nearly zero interseismic slip deficit in the updip portion of the megathrust [*Moreno et al.*, 2012]. Although the resolution of interseismic and postseismic slip is particularly poor there, it is possible that the shallowest portion of the megathrust might creep interseismically. However, *Agurto et al.* [2012] showed that some $M > 4$ earthquakes and associated seismically related afterslip occurred postseismically between March 2010 and March 2012 along the updip edge of the coseismic slip patch south of 35.3° S (also see supporting information). Given the trench-coast distance and the onshore distribution of GPS stations, it is possible that the extent and magnitude of shallow afterslip is beyond the resolution of this study. Our slip potency test (see supporting information) shows that some amount of shallow afterslip cannot be excluded, although the associated slip potency does not exceed $\sim 10\%$ of the total coseismic slip potency.

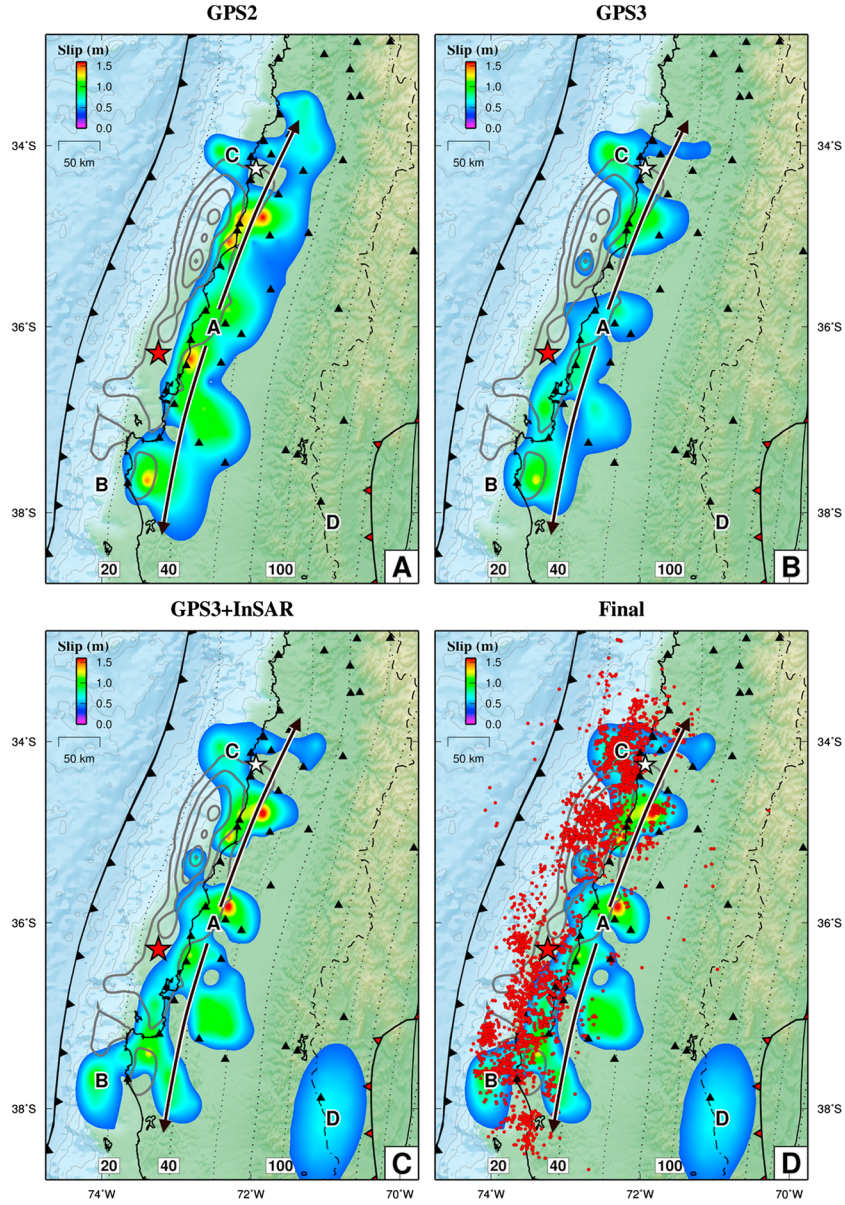


Figure 9. Comparison of the postseismic slip model between the 1st and 488th day constrained by (a) horizontal GPS observations only, (b) all three components of GPS observations, and (c) three component GPS observations plus InSAR data. The coseismic slip model is of 2.5 m contour intervals (gray lines). (d) The same afterslip model as Figure 9c. Red dots are aftershocks [Rietbrock *et al.*, 2012]. Black triangles represent the location of GPS stations. A is the afterslip down-dip of the coseismic slip patch, with the black arrows indicating the along-strike extent. B and C correspond to two regions of afterslip that bound the southern and northern end of the coseismic slip patch. D is a deep slip patch that may reflect some tropospheric errors in the Andes.

6. Discussion

6.1. Postseismic Moment Release

[25] Acknowledging that geodetic data primarily constrain the potency associated with fault slip and not seismic moment, we estimate that the moment released by postseismic slip in 1.3 years is $3.6 \sim 5.1 \cdot 10^{21}$ N·m ($M_w = 8.34 \sim 8.44$), equivalent to 20~30% of the coseismic moment. This ratio is similar to that of earthquakes of similar magnitude, such as the 2001 $M_w = 8.4$ Arequipa earthquake in southern Peru (20~40% in 1 year) [Ruegg *et al.*, 2001; Melbourne *et al.*,

2002] and the 2005 $M_w = 8.7$ Nias earthquake (>25% in 9 month) [Hsu *et al.*, 2006]. The relative magnitude of postseismic to coseismic moment seems to scale with the magnitude of the mainshock (Figure 10a). Smaller earthquakes tend to produce relatively less afterslip, such as the 1995 $M_w = 8.1$ Antofagasta earthquake (<20% in 1 year) [Melbourne *et al.*, 2002; Chlieh *et al.*, 2004; Pritchard and Simons, 2006] and 2007 $M_w = 8.0$ Pisco earthquake (7~28% in 1.1 years) [Perfettini *et al.*, 2010], whereas larger earthquakes tend to have larger values, such as the 2004 $M_w = 9.1$ Sumatra earthquake (30% in the first month and

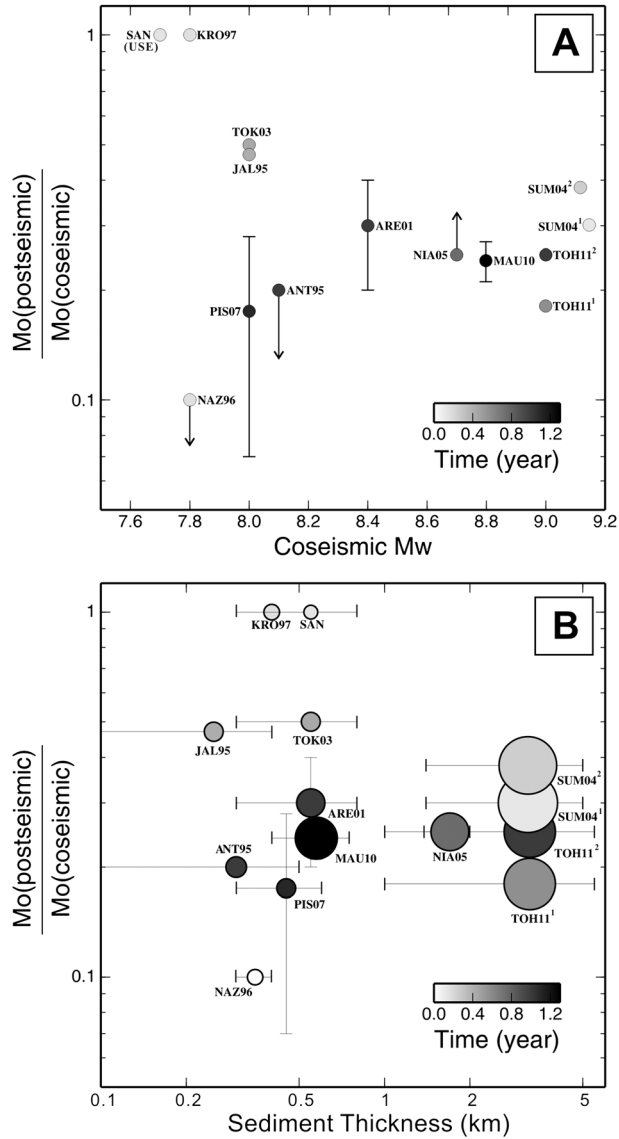


Figure 10. (a) Plot of the estimated postseismic-coseismic ratio as a function of coseismic moment for selected megathrust earthquakes. The ordinate is in log scale to reflect the relationship between M_o and M_w . The color scale of each dot represents the amount of time after the mainshock considered in each postseismic study. The code next to each circle is the first three letters of the event name and its occurrence year: ANT95, 1995 Antofagasta, Chile [Melbourne et al., 2002; Chlieh et al., 2004; Pritchard and Simons, 2006]; ARE01, 2001 Arequipa, Peru [Ruegg et al., 2001; Melbourne et al., 2002]; JAL95, 1995 Jalisco, Mexico [Hutton et al., 2001; Melbourne et al., 2002]; KRO97, 1997 Kronotsky, Kamchatka [Burgmann et al., 2001; Gordeev et al., 2001]; MAU10, 2010 Maule, Chile (this study); NAZ96, 1996 Nazca, Peru [Pritchard et al., 2007]; NIA05, 2005 Nias, Indonesia [Hsu et al., 2006]; PIS07, 2007 Pisco, Peru [Perfettini et al., 2010]; TOH11, 2011 Tohoku, Japan [Ozawa et al., 2012; Geospatial Information Authority of Japan, 2012]; TOK03, 2003 Tokachi-oki, Japan [Miyazaki et al., 2004; Ozawa et al., 2004; Baba et al., 2006]; SAN, 1989–1994 Sanriku-oki, Japan [Kawasaki et al., 1995; Heki et al., 1997; Heki and Tamura, 1997; Nishimura et al., 2000; Kawasaki et al., 2001; Melbourne et al., 2002; Yagi et al., 2003]; SUM04, 2004 Sumatra, Indonesia [Hashimoto et al., 2006; Subarya et al., 2006; Chlieh et al., 2007]. Arrows instead of error bars indicate the circles as the upper bound or lower bound of the values. “USE” under the letters SAN (Sanriku-Oki events) represents “ultraslow earthquake.” (b) Plot of the estimated postseismic-coseismic ratio as a function trench sediment thickness. The size of the circles scales with the mainshock magnitude. Colors of the circles and name codes follow Figure 10a. The sediment thickness estimates are from multiple sources: von Huene and Scholl [1991], Plank and Langmuir [1998], and Divins [2003].

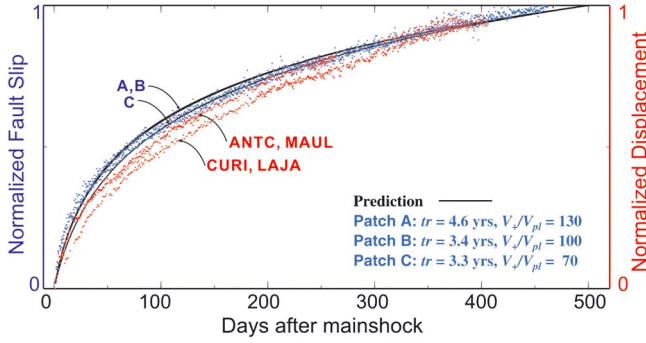


Figure 11. Normalized time-dependent fault slip over different postseismic slip patches from our model result (blue dots; see Figure 9d for locations). The normalized westward displacements over selected GPS stations are also shown for comparison (red dots; see Figure 8 for locations). Solid lines are the model predictions [Perfettini *et al.*, 2010].

38% in 3 months) [e.g., Chlieh *et al.*, 2007] and the 2011 $M_w=9.0$ Tohoku earthquake (18% in 7 months [Ozawa *et al.*, 2012] and $\sim 25\%$ in 1 year [Geospatial Information Authority of Japan, 2012]).

[26] Pritchard and Simons [2006] also pointed out that the amount of sediment subducted may also help modulate the postseismic behavior. As shown in Figure 10b, the relative magnitude of postseismic to coseismic moment increases with sediment thickness, although the correlation is less prominent due to the large variations in trench sediment thickness and the uncertainties in its estimation. We may even attribute the correlation back to the idea that thick trench sediments smooth out the slab topography and encourage large earthquakes [Ruff, 1989]. Such relationship seems to hold in many earthquakes, the most well-known of which is the 1.5 km thick trench sediments in southern Chile and the $M_w=9.5$ 1960 Valdivia earthquake [Scherwath *et al.*, 2009; Contreras-Reyes *et al.*, 2010]. It is therefore difficult to tell which factor, the sediment thickness or the coseismic stress drop, contributes more to the afterslip behavior along the subduction interface.

[27] In both correlation plots, outliers exist. Smaller earthquakes can still be followed by afterslip having a large potency, such as the 1989–1994 Sanriku-oki earthquake sequences in Japan (ranging from $M_w=6.9$ to $M_w=7.7$) [Heki and Tamura, 1997; Kawasaki *et al.*, 2001]. Because the moment release rate is so large (100% in 5–50 days) these postseismic events were further defined as “ultraslow earthquakes” and may likely result from very unique source properties on the subduction interface [Kawasaki *et al.*, 1995]. Other examples include the large afterslip of the 2005–2008 $M_w\sim 7$ earthquakes along the Japan Trench megathrust, whose postseismic moment release exceeded that of the corresponding coseismic events [Suito *et al.*, 2011]. Because the number of earthquakes is small and obvious exceptions exist, more case studies are required to elucidate the possible correlation between the coseismic and postseismic moment release.

6.2. Spatial Friction Variations and the Seismic Barrier

[28] The cumulative moment due to all aftershocks with $M_w > 3$ reported in the National Earthquake Information Center catalogue over the same period of time amounts to

only $5.58e+10^{19}$ N-m, indicating that about 99% of the observed postseismic deformation was aseismic, a value even larger than that of the 2005 Nias earthquake (93%) [Hsu *et al.*, 2006]. Agurto *et al.* [2012] found that in the case of Maule aftershocks, the concentration of larger aftershocks ($M=4\sim 6$) at the boundary between coseismic and postseismic patches illuminates the region with the highest concentration of stress right after the mainshock, and the boundary of the regions of greatest aseismic afterslip. This region is also the loci of a majority of coseismic high-frequency radiators [Lay *et al.*, 2010]. Their spatial distribution depicts the region of frictional heterogeneities within the brittle-ductile transition zone, i.e., small discrete brittle asperities dotted amidst ductile creeping zone [Ito *et al.*, 2007; Simons *et al.*, 2011; Meng *et al.*, 2011]. However, this creeping zone is further bounded by a second band of aftershocks at the downdip margin [Rietbrock *et al.*, 2012], with lobes of afterslip patches sandwiched in between the upper and lower aftershock clusters (Figure 9d), mimicking the complex mosaic of phenomena revealed by the study of the 1995 Antofagasta earthquake in northern Chile and its corresponding afterslip and aftershocks [Pritchard and Simons, 2006]. These deeper aftershocks may result from slip on small stick-slip patches triggered by afterslip. Their locations suggest a nonmonotonic change from a stick-slip regime to a creeping regime with increasing depth.

[29] To explore the frictional properties of the fault patches that produced aseismic afterslip, we compute afterslip with a simple theoretical model. We calculate slip predicted from a one-dimensional rate-strengthening frictional sliding model, assuming that frictional stress increases linearly with the logarithm of the sliding velocity, as observed in laboratory experiments [Marone, 1998]. Based on this model and later analytical derivations [Perfettini and Avouac, 2004; Perfettini *et al.*, 2010], postseismic slip $U(t)$ evolves as

$$U(t) = V_{pl} t_r \log[1 + (V^+/V_{pl} t_r) t] \quad (1)$$

where t is time, V_{pl} is the plate convergence velocity, t_r is the relaxation time, V^+ can be viewed as the creeping velocity during the postseismic period, and the ratio V^+/V_{pl} represents the postseismic creep rate normalized by the long-term plate convergence velocity.

[30] For the elongated region of slip downdip of the coseismic slip patch (patch A in Figure 9), the shallow afterslip offshore of the Arauco Peninsula (patch B), and the afterslip that bounds the coseismic slip patch to the north near San Antonio (patch C), we find a very stable value of t_r of approximately 3.3–4.6 years and V^+/V_{pl} of 70–130 (Figure 11). We further convert V_{pl} and t_r to parameters more closely related to material properties, following the formulation described by Perfettini and Avouac [2004]. Using a value of coseismic Coulomb stress change of 3 MPa for the elongated downdip region, 0.5–1 MPa around the offshore Arauco Peninsula, and 2.5–3 MPa for the northern afterslip patch [Lorito *et al.*, 2011], we find $(a-b)\sigma_n=0.08\text{--}0.62$ MPa for patch A, 0.01–0.22 MPa for patch B, and 0.04–0.65 MPa for patch C, where σ_n denotes effective normal stress, and $a-b$ is the frictional parameter (see Hsu *et al.* [2006] for the steps of obtaining these ranges of $(a-b)\sigma_n$ values).

[31] $a-b$ describes how the coefficient of friction varies as a function of the logarithm of sliding velocity, with positive

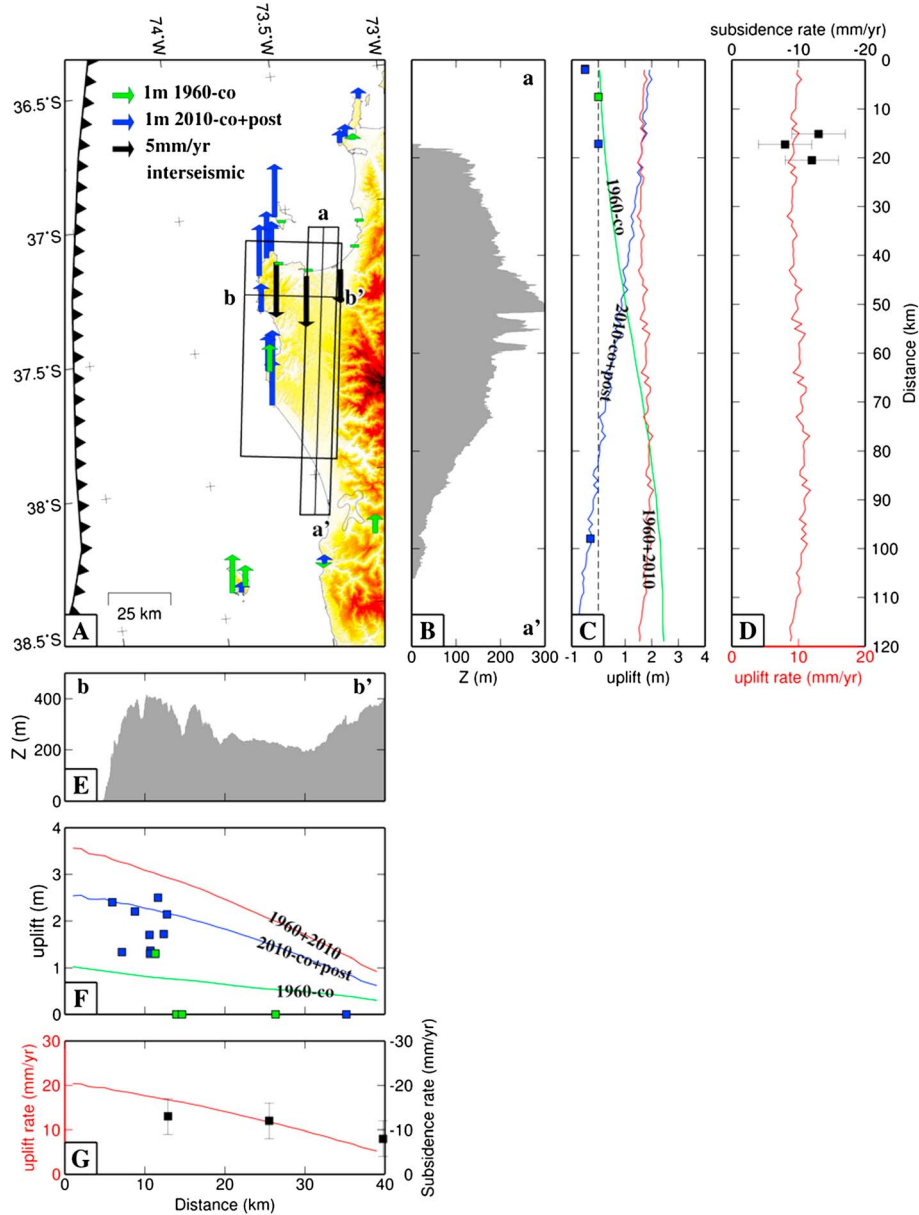


Figure 12. Topography, deformation and uplift/subsidence rate of the Arauco Peninsula along E-W and N-S directions. (a) Map of the Arauco Peninsula. $a-a'$ and $b-b'$ indicate locations of the profiles, with the bounding boxes showing the area of topography being projected onto the profiles. Green vectors and blue vectors are the in situ measurements of coseismic and early postseismic vertical displacement from the 1960 Valdivia earthquake [Plafker and Savage, 1970] and the 2010 Maule earthquake [Vargas *et al.*, 2011]. Black vectors are the vertical velocities from campaign-mode GPS between 1996 and 2002 [Ruegg *et al.*, 2009]. (b) Projected topography along the swath $a-a'$. Vertical exaggeration: 90X. The anticlinal deformation with a WNW-SES trending axis is discussed by Melnick *et al.* [2009]. (c) Coseismic uplift due to the 1960 Valdivia earthquake (green line, Moreno *et al.* [2009]), and the coseismic plus postseismic uplift of the 2010 Maule earthquake (blue line, this study) projected along profile $a-a'$, and the total uplift (red line). Squares are the projected in situ measurements with the same color codes as Figure 12a. Dashed black line indicates the location of the neutral line. (d) The equivalent uplift rate (red line), derived by dividing the total uplift in Figure 12c by the period between 2010 and 1835, assuming the year of 1835 is the onset of another seismic cycle. Black squares are the projected GPS vertical velocities. (e) Projected topography along the swath $b-b'$, showing clear back-tilting of the peninsula. Vertical exaggeration: 25X. (f) Uplift curves along the $b-b'$ profile, with the same color codes as Figure 12c. (g) The equivalent uplift rate and GPS vertical velocities projected along profile $b-b'$.

values corresponding to velocity strengthening and negative values to velocity weakening. The smaller estimated $(a-b)\sigma_n$ value for the offshore Arauco Peninsula and the intermediate value for the northern afterslip patch near San Antonio may result from smaller $a-b$ values than surrounding regions, suggesting strong variations in effective megathrust fault properties in the Arauco and San Antonio intersegment areas. Alternatively, locally high pore pressure and therefore small effective normal stress may play an important role in changing the slip behavior in this region. However, Cubas et al. (in preparation, 2013) use the critical taper theory to infer a values of 0.375–0.6 for the Hubbert-Rubey parameter in these two areas (the ratio of pore pressure versus the lithostatic pressure, with 0.4 for hydrostatic; *Hubbert and Rubey* [1959]), suggesting that the pore pressure is not extraordinarily high in this region. Therefore, it is likely that local frictional heterogeneity (smaller positive $a-b$ values) is responsible for the postseismic creep in the intersegment areas. Numerical modeling of rate-and-state frictional sliding on a shear-loaded planar fault also suggests that when $a-b$ is smaller, postseismic sliding propagates far from the coseismic slip region over short time intervals [*Kato*, 2007].

[32] Compared to intermediate $(a-b)\sigma_n$ values in the San Antonio intersegment area, the nearly neutral inferred value near Arauco might help explain some specific aspects of this area. It has been suggested, based on dynamic modeling of slip on a fault with heterogeneous rate-and-state friction patches, that the barrier effect of a rate-strengthening patch scales with the product of $(a-b)\sigma_n$ and the size of the patch [*Kaneko et al.*, 2010]. It might be argued that because of a relatively small value of $(a-b)\sigma_n$ in the Arauco Peninsula area (0.01–0.22 MPa), dynamic ruptures can propagate into the area but do not rupture through it because of its relatively large size. This effect might explain why we observed both some coseismic slip and aseismic afterslip beneath the Arauco Peninsula area. This inference would also be consistent with seismic slip of ~5 m beneath the Arauco Peninsula during the 1960 Valdivia earthquake [*Moreno et al.*, 2009], although the spatial resolution of the models is very low due to the limited availability of relevant observations. The Arauco Peninsula area would owe its character as a barrier to the size of the modestly rate-strengthening zone. The along-trench length of the Arauco Peninsula barrier is ~100 km, much longer than the Batu Islands barrier in Sumatra [*Chlieh et al.*, 2008] and the Mejillones Peninsula barrier in northern Chile [*Pritchard and Simons*, 2006; *Béjar-Pizarro et al.*, 2010; *Victor et al.*, 2011], which may also be examples of rate-strengthening barriers on subduction megathrusts. The findings from the Arauco Peninsula barrier are consistent with the idea that both the $(a-b)\sigma_n$ value and the barrier size determine the barrier effect of a velocity strengthening patch [*Kaneko et al.*, 2010].

6.3. Arauco Peninsula Uplift

[33] We now consider the timing of the deformation of the peninsula in the context of the seismic cycle. If we assume that the whole medium is purely elastic, all elastic strain that accumulates during the interseismic period should be released in earthquakes. In this case, there is no permanent strain and no formation of the peninsula. Clearly, inelastic deformation must have occurred or be occurring to account for the uplift of the Arauco Peninsula. *Melnick et al.* [2009]

suggested that there are two styles of long-term deformation on the peninsula: anticlinal bending (Figure 12b), with the anticline axis going through the center of the peninsula in a WNW-ESE orientation, and back tilting, with the marine terraces tilting toward the east (Figure 12e). We now compare these deformation styles to the geodetic data and modeled results we obtained during the past two decades. Because of the lack of in situ measurements within the swath along the profile $a-a'$, we use only the modeled uplift to derive the total uplift between 1835 and 2010 (Figure 12c). Using the elapsed time of 175 years, the equivalent interseismic uplift rate is nearly equivalent to the measured subsidence rate (Figure 12d). The nearly neutral balance seems to indicate that all the elastic strain has been released during the two large earthquakes and no permanent strain has accumulated within the last seismic cycle. However, based on the estimates from *Melnick et al.* [2009], the long-term uplift rate ranges from 1.8 mm/yr near the anticline axis to 0.3 mm/yr near the bottom of the anticline flank. The difference is so small (1.5 mm/yr) that it resides within the errors of model predictions and the GPS observations. In this case, we probably would not be able to isolate coseismic or interseismic nonelastic deformation of the anticline on the Arauco Peninsula.

[34] Along profile $b-b'$, the uplift pattern from model predictions agrees in general with field observations (Figure 12f), and the cumulative coseismic deformation since 1835 mimics the back-tilting of the peninsula. The equivalent uplift rate during the past 175 years is slightly larger than the interseismic subsidence as we get close to the trench, resulting in backtilt-like deformation (Figure 12g). A straightforward interpretation is that the backtilting of the peninsula may form during the coseismic and early postseismic periods, although it is not clear whether the anticlinal folding should also happen at the same time. This permanent nonelastic deformation could be either associated with the elastic cycle on the megathrust, or resulting from the slip on crustal splay faults in the frontal accretionary prism (Figure 1b) [*Contreras-Reyes et al.*, 2010; *Melnick et al.*, 2012]. As the chance of rupture propagation into this area increases due to low inferred $(a-b)\sigma_n$ values, so does the triggered slip on the crustal splay faults, and the accumulation of nonelastic deformation. This idea of coseismic and postseismic uplift of the Arauco Peninsula is different from the observations around the Mejillones Peninsula in northern Chile [*Ortlieb et al.*, 1996; *Pritchard and Simons*, 2006; *Loveless et al.*, 2010] and the Paracas Peninsula in Peru [*Sladen et al.*, 2010], whose patterns of coseismic vertical movement are different from that of the long-term deformation. The behavior of these peninsulas is considered to be dominated by postseismic and interseismic uplift [*Sladen et al.*, 2010; *Victor et al.*, 2011]. An alternative interpretation is that the backtilting of the Arauco Peninsula results from a deficit of interseismic subsidence, which in turn is the net effect of elastic subsidence and nonelastic uplift in the interseismic period. The coeval strain accumulation of opposite signs is a more complicated interpretation, and therefore field evidence is needed to support this view.

6.4. Limitations

[35] We summarize here all the discrepancies between observations and predictions, together with the anomalies in our model. First, our favored coseismic slip model fails to predict the short-wavelength signals in the GPS vertical

component (Figure 6), which can be fit only when allowing deep slip patches beneath the Andes [Vigny *et al.*, 2011]. Second, there is a systematic misfit in postseismic horizontal displacements for GPS stations around the Andes (Figure 8). These stations demonstrate different deformation behaviors from the three major afterslip patches (Figure 11). These results suggest that the middle- to far-field sampling of the deformation field associated with the Maule earthquake will require more realistic models than elastic or layered elastic half-space.

[36] The above-mentioned discrepancies and model anomalies can be potentially explained by one or more of the following: (1) over-simplification of the elastic model, (2) elastic deformation along other uppercrustal structures, and (3) deformation due to other mechanisms, such as viscoelastic deformation. We address these issues separately below.

[37] As demonstrated earlier, adopting a homogeneous elastic half-space or a 1-D layered elastic half-space can modulate the inferred patterns of fault slip (Figure S8). Hsu *et al.* [2011] have pointed out the important role played by 3-D elastic structure in fault slip inversions. Based on heat flow observations and numerical models, Volker *et al.* [2011] estimated that the geothermal gradient varies greatly over a distance of 400 km, from 10°C/km near the coast, to 5.5°C/km near the Central Valley, and to 22.5°C/km below the Andes. Given the temperature and compositional dependence of elastic moduli, we may expect considerable 3-D variations in elastic structure. Future models of this region using 3-D elastic Green's functions may help us understand the discrepancies—although our relatively poor a priori understanding of 3-D elastic structure may make such an effort pointless.

[38] We are also concerned with the potential role played by upper-crustal structure(s) during and after the earthquake. This explanation for the misfits proximal to the Andes may be as viable as that of variations in 3-D elastic structure, although elastic deformation associated with the earthquake cycle at the plate boundary will not result in the permanent deformation that built the Andes. Slip on a shallow crustal fault, or a downdip extension of such a fault, will create permanent surface deformation of a smaller spatial wavelength similar to the depth of the dislocation tip, a pattern that we see in the coseismic vertical displacement field. Given the locations of the GPS stations with large misfits across the Andes (Figure 8), the Neogene Deformation Front, the west-vergent thrust faults that bounds the west flank of the Andes (between 32° and 38°S, Figures 1b and 1c) and their associated décollement may be potential candidates for such an aseismically slipping upper crustal structure (Figure 1c) [Armijo *et al.*, 2010]. The Quaternary deformation pattern along this fault system has long been a subject of debate. There appears to be little indication of Quaternary contraction except along a small section of Southern Central Andes (36°–38°S) [Folguera and Ramos, 2009]. Folguera *et al.* [2007, 2008] even argue that an extensional state of stress in the Andean Cordillera and foothills is producing a regional collapse. On the other hand, Cobbold and Rossello [2003], Galland *et al.* [2007], Guzmán *et al.* [2007], and Messenger *et al.* [2010] postulate that the stress regime remains mainly compressive. If this shallow crustal fault hypothesis holds, its associated surface deformation will still be intertwined with deformation from the interaction on the plate boundary, making it nontrivial to separate the relative

contribution from each structure. A denser and more optimally designed GPS network may be needed to specifically target these upper plate structures. We recognize that considerably more study is needed to characterize the role, if any, of hypothesized upper crustal structures, how they are driven by the plate boundary, and how they contribute to the nonelastic deformation that creates the Andes.

[39] It is also possible that viscoelastic deformation may account for a non-negligible part of the observed postseismic deformation [e.g., Pollitz *et al.*, 1998, 2006]. Nevertheless, because viscoelastic deformation is triggered by coseismic stress change and acts mainly during the postseismic period, this process alone will not reconcile the discrepancies between the observed short-wavelength and modeled long-wavelength coseismic vertical deformation. It is likely that the combination of two or more of the aforementioned processes is necessary to explain all the coseismic and postseismic data for the Maule earthquake.

[40] These discrepancies between our models and the data have significant implications. The Maule earthquake produced measureable deformation in the overriding plate out to a distance of over 1000 km. The standard coseismic and postseismic modeling of such events using layered elastic half-space produces results that explain observations in western Chile well. Our models are less successful in explaining observations in central and eastern Chile and all of Argentina. Such observations, which are not available when the overriding plate consists of a relatively narrow island chain (such as Sumatra and Japan), will potentially provide the data needed to differentiate between competing models for postseismic behavior.

7. Conclusions

[41] To summarize, our joint inversion model shows a coseismic slip pattern similar to the previous ones derived from joint inversion of seismic, geodetic and tsunami data [Delouis *et al.*, 2010; Lorito *et al.*, 2011]. The shallowest 15–20 km of the megathrust shows neither significant coseismic slip nor resolvable postseismic slip, suggesting that the slip on this portion of the megathrust is dominantly due to interseismic creep (between 1835 and 2010). Slip on the megathrust at depth between 15–20 and 50 km is probably mostly seismic. An exception is near the Arauco Peninsula, where aseismic afterslip extends to as shallow as 10 km near trench. We derive a nearly neutral $a-b$ value for this shallow afterslip patch, consistent with the inferred propagation of seismic rupture into this region, whereas the large width of this segment boundary would be the main reason for its barrier effect. This conditionally stable characteristic may also be related to the coseismic uplift of the Arauco Peninsula, as seismic ruptures may propagate more easily into this barrier and trigger the slip on upper-crust structures. Postseismic energy release follows a general trend in which the amount of postseismic slip scales with the coseismic moment release. Our result also shows marked data misfit near the Andes, indicating that other geophysical processes may be involved in the postseismic deformation over the region.

[42] **Acknowledgments.** We thank Matthew Pritchard, the other reviewer and the associate editor of *JGR-Solid Earth*, for valuable comments and suggestions. We thank Shengji Wei at Caltech for providing the

coseismic deformation model for the Pichilemu aftershock. We also thank Nadaya Cubas for her valuable discussions and help in interpreting the frictional properties. ALOS data is copyright Japanese Aerospace Exploration Agency and METI and provided through the U.S. Government Research Consortium Data Pool at the Alaska Satellite Facility and through the Group on Earth Observation Geohazards Supersite. This research is co-funded by NSF grant EAR-1118239, the Gordon and Betty Moore Foundation through Grant GBMF #423.01 to the Caltech Tectonics Observatory, and the NASA Earth Surface and Interior focus area and carried out at the Jet Propulsion Laboratory, California Institute of Technology, under a contract with the National Aeronautics and Space Administration. Part of the cGPS data used for this study have been acquired under the Chilean-French international collaboration "LIA Montessus de ballore," supported by CONICYT and CNRS; and ANR project SUBCHILE (grant #ANR-05-CATT-014). This paper is Caltech Tectonic Observatory contribution 211 and Seismolab contribution 10088.

References

- Agurto, H., A. Rietbrock, I. Ryder, and M. Miller (2012), Seismic-afterslip characterization of the 2010 MW 8.8 Maule, Chile, earthquake based on moment tensor inversion, *Geophys. Res. Lett.*, *39*, L20303, doi:10.1029/2012GL053434.
- Armijo, R., R. Rauld, R. Thiele, G. Vargas, J. Campos, R. Lacassin, and E. Kausel (2010), The West Andean Thrust, the San Ramon Fault, and the seismic hazard for Santiago, Chile, *Tectonics*, *29*, TC2007, doi:10.1029/2008TC002427.
- Astroza, M., F. Cabezas, M. O. Moroni, L. Massone, S. Ruiz, E. Parra, F. Cordero, and A. Mottadelli (2010), Intensidades sísmicas en el área de daños del terremoto del 27 de Febrero de 2010, Departamento de Ingeniería Civil, Facultad de Ciencias Físicas y Matemáticas, Universidad de Chile.
- Baba, T., K. Hirata, T. Hori, and H. Sakaguchi (2006), Offshore geodetic data conducive to the estimation of the afterslip distribution following the 2003 Tokachi-oki earthquake, *Earth Planet. Sci. Lett.*, *241*, 281–292, doi:10.1016/j.epsl.2005.10.019.
- Barrientos, S. E., and S. N. Ward (1990), The 1960 Chile earthquake: inversion for slip distribution from surface deformation, *Geophys. J. Int.*, *103*(3), 589–598.
- Beck, S., S. Barrientos, E. Kausel, and M. Reyes (1998), Source characteristics of historic earthquakes along the central Chile subduction zone, *J. S. Am. Earth Sci.*, *11*(2), 115–129.
- Béjar-Pizarro, M., et al. (2010), Asperities and barriers on the seismogenic zone in North Chile: state-of-the-art after the 2007 Mw 7.7 Tocopilla earthquake inferred by GPS and InSAR data, *Geophys. J. Int.*, *183*(1), 390–406, doi:10.1111/j.1365-246X.2010.04748.x.
- Burgmann, R., M. G. Kogan, V. E. Levin, C. H. Scholz, R. W. King, and G. M. Steblov (2001), Rapid aseismic moment release following the 5 December, 1997 Kronotsky, Kamchatka, earthquake, *Geophys. Res. Lett.*, *28*(7), 1331–1334, doi:10.1029/2000gl012350.
- Cahill, T., and B. L. Isacks (1992), Seismicity and Shape of the Subducted Nazca Plate, *J. Geophys. Res.*, *97*(B12), 17503–17529, doi:10.1029/92jb00493.
- Campos, J., D. Hatzfeld, R. Madariaga, G. Lopez, E. Kausel, A. Zollo, G. Iannacone, R. Fromm, S. Barrientos, and H. Lyon-Caen (2002), A seismological study of the 1835 seismic gap in south-central Chile, *Phys. Earth Planet. In.*, *132*(1–3), 177–195, doi:10.1016/S0031-9201(02)00051-1.
- Chlieh, M., J. B. De Chabaliér, J. C. Ruegg, R. Armijo, R. Dmowska, J. Campos, and K. L. Feigl (2004), Crustal deformation and fault slip during the seismic cycle in the North Chile subduction zone, from GPS and InSAR observations, *Geophys. J. Int.*, *158*(2), 695–711, doi:10.1111/j.1365-246X.2004.02326.x.
- Chlieh, M., et al. (2007), Coseismic slip and afterslip of the great M(w) 9.15 Sumatra-Andaman earthquake of 2004, *B. Seismol. Soc. Am.*, *97*(1), S152–S173, doi:10.1785/0120050631.
- Chlieh, M., J. P. Avouac, K. Sieh, D. H. Natawidjaja, and J. Galetzka (2008), Heterogeneous coupling of the Sumatran megathrust constrained by geodetic and paleogeodetic measurements, *J. Geophys. Res.*, *113*(B5), B05305, doi:10.1029/2007jb004981.
- Cifuentes, I. L. (1989), The 1960 Chilean Earthquakes, *J. Geophys. Res.*, *94*(B1), 665–680.
- Cisternas, M., et al. (2005), Predecessors of the giant 1960 Chile earthquake, *Nature*, *437*(7057), 404–407, doi:10.1038/nature03943.
- Cobbold, P. R., and E. A. Rossello (2003), Aptian to recent compressional deformation, foothills of the Neuquen Basin, Argentina, *Mar. Pet. Geol.*, *20*(5), 429–443, doi:10.1016/S0264-8172(03)00077-1.
- Contreras-Reyes, E., E. R. Flueh, and I. Grevemeyer (2010), Tectonic control on sediment accretion and subduction off south central Chile: Implications for coseismic rupture processes of the 1960 and 2010 megathrust earthquakes, *Tectonics*, *29*, TC6018, doi:10.1029/2010TC002734.
- Darwin, C. (1851), *Geological Observations on Coral Reefs, Volcanic Islands, and on South America – Being the Geology of the Voyage of the Beagle, Under the Command of Captain Fitzroy, R.N., During the Years 1832 to 1836*, p. 768, Smith, Elder, and Co., London, U.K.
- Delouis, B., J.-M. Nocquet, and M. Vallee (2010), Slip distribution of the February 27, 2010 Mw = 8.8 Maule Earthquake, central Chile, from static and high-rate GPS, InSAR, and broadband teleseismic data, *Geophys. Res. Lett.*, *37*, L17305, doi:10.1029/2010GL043899.
- Divins, D. L. (2003), *Total Sediment Thickness of the World's Oceans and Marginal Seas*, edited by N. N. G. D. Center, Boulder, Colo.
- Fariás, M., G. Vargas, A. Tassara, S. Carretier, S. Baize, D. Melnick, and K. Bataille (2010), Land-level changes produced by the Mw 8.8 2010 Chilean earthquake, *Science*, *329*(5994), 916, doi:10.1126/science.1192094.
- Folguera, A., and V. A. Ramos (2009), Collision of the Mocha fracture zone and a < 4 Ma old wave of orogenic uplift in the Andes (36°–38°S), *Lithosphere*, *1*(6), 364–369, doi:10.1130/L66.1.
- Folguera, A., V. A. Ramos, R. L. Hermanns, and J. Naranjo (2004), Neotectonics in the foothills of the southernmost central Andes (37°–38°S): Evidence of strike-slip displacement along the Antinir-Copahue fault zone, *Tectonics*, *23*(5), TC5008, doi:10.1029/2003TC001533.
- Folguera, A., A. Introcaso, M. Giménez, F. Ruiz, P. Martínez, C. Tunstall, E. García Morabito, and V. A. Ramos (2007), Crustal attenuation in the Southern Andean retroarc (38°–39°30'S) determined from tectonic and gravimetric studies: The Lonco-Luán asthenospheric anomaly, *Tectonophysics*, *439*, 129–147, doi:10.1016/j.tecto.2007.04.001.
- Folguera, A., G. Bottesi, T. Zapata, and V. A. Ramos (2008), Crustal collapse in the Andean backarc since 2 Ma: Tromen volcanic plateau, Southern Central Andes (36°40'–37°30'), *Tectonophysics*, *459*, 140–160, doi:10.1016/j.tecto.2007.12.013.
- Fritz, H., et al. (2011), Field survey of the 27 February 2010 Chile tsunami, *Pure Appl. Geophys.*, *168*(11), 1989–2010, doi:10.1007/s00024-011-0283-5.
- Galland, O., E. Hallot, P. R. Cobbold, G. Ruffet, and J. de Bremond d'Arce (2007), Volcanism in a compressional Andean setting: A structural and geochronological study of Tromen volcano (Neuquén province, Argentina), *Tectonics*, *26*, TC4010, doi:10.1029/2006TC002011.
- Geospatial Information Authority of Japan (2012), Postseismic slip distribution model inferred from GEONET data, edited, Japan.
- Gordeev, E. I., A. A. Gusev, V. E. Levin, V. F. Bakhtiarov, V. M. Pavlov, V. N. Chebrov, and M. Kasahara (2001), Preliminary analysis of deformation at the Eurasia-Pacific-North America plate junction from GPS data, *Geophys. J. Int.*, *147*(1), 189–198, doi:10.1046/j.0956-540x.2001.01515.x.
- Guzmán, C., E. Cristallini, and G. Bottesi (2007), Contemporary stress orientations in the Andean retroarc between 34°S and 39°S from borehole breakout analysis, *Tectonics*, *26*, TC3016, doi:10.1029/2006TC001958.
- Haberland, C., A. Rietbrock, D. Lange, K. Bataille, and T. Dahm (2009), Structure of the seismogenic zone of the southcentral Chilean margin revealed by local earthquake traveltome tomography, *J. Geophys. Res.*, *114*, B01317, doi:10.1029/2008JB005802.
- Hashimoto, M., N. Choosakul, M. Hashizume, S. Takemoto, H. Takiguchi, Y. Fukuda, and K. Frjimori (2006), Crustal deformations associated with the great Sumatra-Andaman earthquake deduced from continuous GPS observation, *Earth Planets Space*, *58*(2), 127–139.
- Hébert, H., P. Heinrich, S. François, and A. Piatanesi (2001), Far-field simulation of tsunami propagation in the Pacific Ocean: impact on the Marquesas Islands (French Polynesia), *J. Geophys. Res.*, *106*(C5), 9161–9177, doi:10.1029/2000JC000552.
- Heinrich, P., F. Schindele, S. Guibourg, and F. P. Ihlmlé (1998), Modeling of the February 1996 Peruvian tsunami, *Geophys. Res. Lett.*, *25*(14), 2687–2690.
- Heki, K., and Y. Tamura (1997), Short term afterslip in the 1994 Sanriku-Haruka-Oki earthquake, *Geophys. Res. Lett.*, *24*(24), 3285–3288, doi:10.1029/97gl03316.
- Heki, K., S. Miyazaki, and H. Tsuji (1997), Silent fault slip following an interplate thrust earthquake at the Japan Trench, *Nature*, *386*(6625), 595–598, doi:10.1038/386595a0.
- Hsu, Y.-J., M. Simons, J.-P. Avouac, J. Galetzka, K. Sieh, M. Chlieh, D. Natawidjaja, L. Prawirodirdjo, and Y. Bock (2006), Frictional afterslip following the 2005 Nias-Simeulue earthquake, Sumatra, *Science*, *312*(5782), 1921–1926, doi:10.1126/science.1126960.
- Hsu, Y.-J., M. Simons, C. Williams, and E. Casarotti (2011), Three-dimensional FEM derived elastic Green's functions for the coseismic deformation of the 2005 Mw 8.7 Nias-Simeulue, Sumatra earthquake, *Geochem. Geophys. Geosyst.*, *12*, Q07013, doi:10.1029/2011GC003553.
- Hubbert, M. K., and W. W. Rubey (1959), Role of fluid pressure in mechanics of overthrust faulting. I. Mechanics of fluid-filled porous solids and its application to overthrust faulting, *Geol. Soc. Am. Bull.*, *70*(2), 115–166.

- von Huene, R., and D. W. Scholl (1991), Observations at convergent margins concerning sediment subduction, subduction erosion, and the growth of continental crust, *Rev. Geophys.*, 29(3), 279–316.
- Hutton, W., C. DeMets, O. Sanchez, G. Suarez, and J. Stock (2001), Slip kinematics and dynamics during and after the 1995 October 9 M_w=8.0 Colima-Jalisco earthquake, Mexico, from GPS geodetic constraints, *Geophys. J. Int.*, 146(3), 637–658, doi:10.1046/j.1365-246X.2001.00472.x.
- Ito, Y., K. Obara, K. Shiomi, S. Sekine, and H. Hirose (2007), Slow earthquakes coincident with episodic tremors and slow slip events, *Science*, 315(5811), 503–506, doi:10.1126/science.1134454.
- Ji, C., D. J. Wald, and D. V. Helmberger (2002), Source description of the 1999 Hector Mine, California, earthquake, part I: Wavelet domain inversion theory and resolution analysis, *B. Seismol. Soc. Am.*, 92(4), 1192–1207, doi:10.1785/0120000916.
- Kaneko, Y., J.-P. Avouac, and N. Lapusta (2010), Towards inferring earthquake patterns from geodetic observations of interseismic coupling, *Nat. Geosci.*, 3(5), 363–369, doi:10.1038/NGEO843.
- Kato, N. (2007), Expansion of aftershock areas caused by propagating post-seismic sliding, *Geophys. J. Int.*, 168(2), 797–808, doi:10.1111/j.1365-246X.2006.03255.x.
- Kawasaki, I., Y. Asai, Y. Tamura, T. Sagiya, N. Mikami, Y. Okada, M. Sakata, and M. Kasahara (1995), The 1992 Sanriku-oki, Japan, ultra-slow earthquake, *J. Phys. Earth*, 43(2), 105–116.
- Kawasaki, I., Y. Asai, and Y. Tamura (2001), Space-time distribution of interplate moment release including slow earthquakes and the seismogeodetic coupling in the Sanriku-oki region along the Japan trench, *Tectonophysics*, 330(3–4), 267–283, doi:10.1016/S0040-1951(00)00245-6.
- Kendrick, E., M. Bevis, R. Smalley, B. Brooks, R. B. Vargas, E. Lauria, and L. P. S. Fortes (2003), The Nazca South America Euler vector and its rate of change, *J. S. Am. Earth Sci.*, 16(2), 125–131, doi:10.1016/S0895-9811(03)00028-2.
- Konca, A. O., et al. (2008), Partial rupture of a locked patch of the Sumatra megathrust during the 2007 earthquake sequence, *Nature*, 456(7222), 631–635, doi:10.1038/nature07572.
- Kositsky, A., and J. P. Avouac (2010), Inverting geodetic time-series with a principal component analysis-based inversion method (PCAIM), *J. Geophys. Res.*, 115, B03401, doi:10.1029/2009JB006535.
- Lay, T., C. J. Ammon, H. Kanamori, K. D. Koper, O. Sufri, and A. R. Hutko (2010), Teleseismic inversion for rupture process of the 27 February 2010 Chile (M_w 8.8) earthquake, *Geophys. Res. Lett.*, 37, L13301, doi:10.1029/2010GL043379.
- Lin, Y.-n. N., A. P. Kositsky, and J.-P. Avouac (2010), PCAIM joint inversion of InSAR and ground-based geodetic time series: Application to monitoring magmatic inflation beneath the Long Valley Caldera, *Geophys. Res. Lett.*, 37, L23301, doi:10.1029/2010GL045769.
- Lomnitz, C. (2004), Major earthquakes of Chile: A historical survey, 1535-1960, *Seismol. Res. Lett.*, 75(3), 368–378.
- Lorito, S., F. Romano, S. Atzori, X. Tong, A. Avallone, J. McCloskey, M. Cocco, E. Boschi, and A. Piatanesi (2011), Limited overlap between the seismic gap and coseismic slip of the great 2010 Chile earthquake, *Nat. Geosci.*, 4(3), 173–177, doi:10.1038/NGEO1073.
- Loveless, J. P., M. E. Pritchard, and N. Kukowski (2010), Testing mechanisms of subduction zone segmentation and seismogenesis with slip distributions from recent Andean earthquakes, *Tectonophysics*, 495(1–2), 15–33, doi:10.1016/j.tecto.2009.05.008.
- Madariaga, R., M. Métois, C. Vigny, and J. Campos (2010), Central Chile finally breaks, *Science*, 328(5975), 181–182, doi:10.1126/science.1189197.
- Marone, C. (1998), Laboratory-derived frictional laws and their application to seismic faulting, *Annu. Rev. Earth Planet. Sci.*, 26(1), 643–696, doi:10.1146/annurev.earth.26.1.643.
- Melbourne, T. I., F. H. Webb, J. M. Stock, and C. Reigber (2002), Rapid postseismic transients in subduction zones from continuous GPS, *J. Geophys. Res.*, 107(B10), 2241, doi:10.1029/2001JB000555.
- Melnick, D., B. Bookhagen, M. R. Strecker, and H. P. Echter (2009), Segmentation of megathrust rupture zones from fore-arc deformation patterns over hundreds to millions of years, Arauco peninsula, Chile, *J. Geophys. Res.*, 114, B01407, doi:10.1029/2008JB005788.
- Melnick, D., M. Moreno, M. Motagh, M. Cisternas, and R. L. Wesson (2012), Splay fault slip during the Mw 8.8 2010 Maule Chile earthquake, *Geology*, doi:10.1130/G32712.1.
- Meng, L., A. Inbal, and J.-P. Ampuero (2011), A window into the complexity of the dynamic rupture of the 2011 Mw 9 Tohoku-Oki earthquake, *Geophys. Res. Lett.*, 38, L00G07, doi:10.1029/2011GL048118.
- Messenger, G., B. Niviere, J. Martinod, P. Lacan, and J. P. Xavier (2010), Geomorphic evidence for Plio-Quaternary compression in the Andean foothills of the southern Neuquén Basin, Argentina, *Tectonics*, 29, TC4003, doi:10.1029/2009TC002609.
- Métois, M., A. Socquet, and C. Vigny (2012), Interseismic coupling, segmentation and mechanical behavior of the central Chile subduction zone, *J. Geophys. Res.*, 117, B03406, doi:10.1029/2011jb008736.
- Miyazaki, S., P. Segall, J. Fukuda, and T. Kato (2004), Space time distribution of afterslip following the 2003 Tokachi-oki earthquake: Implications for variations in fault zone frictional properties, *Geophys. Res. Lett.*, 31, L06623, doi:10.1029/2003GL019410.
- Moreno, M. S., J. Klotz, D. Melnick, H. Echter, and K. Bataille (2008), Active faulting and heterogeneous deformation across a megathrust segment boundary from GPS data, south central Chile (36–39°S), *Geochem. Geophys. Geosyst.*, 9, Q12024, doi:10.1029/2008GC002198.
- Moreno, M. S., J. Bolte, J. Klotz, and D. Melnick (2009), Impact of megathrust geometry on inversion of coseismic slip from geodetic data: Application to the 1960 Chile earthquake, *Geophys. Res. Lett.*, 36, L16310, doi:10.1029/2009GL039276.
- Moreno, M., M. Rosenau, and O. Oncken (2010), 2010 Maule earthquake slip correlates with pre-seismic locking of Andean subduction zone, *Nature*, 467(7312), 198–202, doi:10.1038/nature09349.
- Moreno, M., et al. (2012), Toward understanding tectonic control on the Mw 8.8 2010 Maule Chile earthquake, *Earth Planet. Sci. Lett.*, 321–322, 152–165, doi:10.1016/j.epsl.2012.01.006.
- Nishimura, T., et al. (2000), Distribution of seismic coupling on the subducting plate boundary in northeastern Japan inferred from GPS observations, *Tectonophysics*, 323(3–4), 217–238, doi:10.1016/S0040-1951(00)00108-6.
- Ortlieb, L., S. Barrientos, and N. Guzman (1996), Coseismic coastal uplift and coralline algae record in Northern Chile: The 1995 Antofagasta earthquake case, *Quat. Sci. Rev.*, 15(8–9), 949–960, doi:10.1016/S0277-3791(96)00056-X.
- Ozawa, S., M. Kaidzu, M. Murakami, T. Imakiire, and Y. Hatanaka (2004), Coseismic and postseismic crustal deformation after the Mw 8 Tokachi-oki earthquake in Japan, *Earth Planets Space*, 56(7), 675–680.
- Ozawa, S., T. Nishimura, H. Munekane, H. Suito, T. Kobayashi, M. Tobita, and T. Imakiire (2012), Preceding, coseismic, and postseismic slips of the 2011 Tohoku earthquake, Japan, *J. Geophys. Res.*, 117, B07404, doi:10.1029/2011JB009120.
- Perfettini, H., and J. P. Avouac (2004), Postseismic relaxation driven by brittle creep: A possible mechanism to reconcile geodetic measurements and the decay rate of aftershocks, application to the Chi-Chi earthquake, Taiwan, *J. Geophys. Res.*, 109, B02304, doi:10.1029/2003JB002488.
- Perfettini, H., et al. (2010), Seismic and aseismic slip on the Central Peru megathrust, *Nature*, 465(7294), 78–81, doi:10.1038/nature09062.
- Piatanesi, A., and S. Lorito (2007), Rupture process of the 2004 Sumatra-Andaman earthquake from tsunami waveform inversion, *B. Seismol. Soc. Am.*, 97(1), S223–S231, doi:10.1785/0120050627.
- Plafker, G., and J. C. Savage (1970), Mechanism of the Chilean Earthquakes of May 21 and 22, 1960, *Geol. Soc. Am. Bull.*, 81(4), 1001–1030.
- Plank, T., and C. H. Langmuir (1998), The chemical composition of subducting sediment and its consequences for the crust and mantle, *Chem. Geol.*, 145(3–4), 325–394.
- Pollitz, F. F., R. Burgmann, and P. Segall (1998), Joint estimation of afterslip rate and postseismic relaxation following the 1989 Loma Prieta earthquake, *J. Geophys. Res.*, 103(B11), 26975–26992, doi:10.1029/98jb01554.
- Pollitz, F. F., R. Burgmann, and P. Banerjee (2006), Post-seismic relaxation following the great 2004 Sumatra-Andaman earthquake on a compressible self-gravitating Earth, *Geophys. J. Int.*, 167(1), 397–420, doi:10.1111/j.1365-246X.2006.03018.x.
- Pritchard, M. E., and M. Simons (2006), An aseismic slip pulse in northern Chile and along-strike variations in seismogenic behavior, *J. Geophys. Res.*, 111(B8), B08405, doi:10.1029/2006JB004258.
- Pritchard, M. E., E. O. Norabuena, C. Ji, R. Boroscchek, D. Comte, M. Simons, T. H. Dixon, and P. A. Rosen (2007), Geodetic, teleseismic, and strong motion constraints on slip from recent southern Peru subduction zone earthquakes, *Journal of Geophysical Research: Solid Earth*, 112, B03307, doi:10.1029/2006jb004294.
- Rietbrock, A., C. Haberland, K. Bataille, T. Dahm, and O. Oncken (2005), Studying the seismogenic coupling zone with a passive seismic array, *Eos. Trans. AGU*, 86, 293–300, doi:10.1029/2005EO320001.
- Rietbrock, A., I. Ryder, G. Hayes, C. Haberland, D. Comte, S. Roecker, and H. Lyon-Caen (2012), Aftershock seismicity of the 2010 Maule Mw = 8.8, Chile, earthquake: Correlation between co-seismic slip models and aftershock distribution?, *Geophys. Res. Lett.*, 39, L08310, doi:10.1029/2012GL051308.
- Ruegg, J. C., M. Olcay, and D. Lazo (2001), Co-, post- and pre(?) seismic displacements associated with the Mw 8.4 Southern Peru Earthquake of 23 June 2001 from continuous GPS measurements, *Seismol. Res. Lett.*, 72(6), 673–678, doi:10.1785/gssrl.72.6.673.
- Ruegg, J. C., J. Campos, R. Madariaga, E. Kausel, J. B. de Chabaliere, R. Armijo, D. Dimitrov, I. Georgiev, and S. Barrientos (2002), Interseismic strain

- accumulation in south central Chile from GPS measurements, 1996-1999, *Geophys. Res. Lett.*, 29(11), 1517, doi:10.1029/2001GL013438.
- Ruegg, J. C., A. Rudloff, C. Vigny, R. Madariaga, J. B. de Chabaliar, J. Campos, E. Kausel, S. Barrientos, and D. Dimitrov (2009), Interseismic strain accumulation measured by GPS in the seismic gap between Constitución and Concepción in Chile, *Phys. Earth Planet. Inter.*, 175(1-2), 78-85, doi:10.1016/j.pepi.2008.02.015.
- Ruff, L. J. (1989), Do trench sediments affect great earthquake occurrence in subduction zones?, *Pure Appl. Geophys.*, 129(1-2), 263-282, doi:10.1007/bf00874629.
- Satake, K. (1993), Depth distribution of coseismic slip along the Nankai Trough, Japan, from joint inversion of geodetic and tsunami data, *Journal of Geophysical Research: Solid Earth*, 98(B3), 4553-4565, doi:10.1029/92jb01553.
- Scherwath, M., E. Contreras-Reyes, E. R. Flueh, I. Grevemeyer, A. Krabbenhoft, C. Papenberg, C. J. Petersen, and R. W. Weinrebe (2009), Deep lithospheric structures along the southern central Chile margin from wide-angle P-wave modelling, *Geophys. J. Int.*, 179(1), 579-600, doi:10.1111/j.1365-246X.2009.04298.x.
- Simons, M., et al. (2011), The 2011 magnitude 9.0 Tohoku-Oki earthquake: Mosaicking the megathrust from seconds to centuries, *Science*, 332(6036), 1421-1425, doi:10.1126/science.1206731.
- Sladen, A., and H. Hébert (2008), On the use of satellite altimetry to infer the earthquake rupture characteristics: application to the 2004 Sumatra event, *Geophys. J. Int.*, 172(2), 707-714, doi:10.1111/j.1365-246X.2007.03669.x.
- Sladen, A., H. Tavera, M. Simons, J. P. Avouac, A. O. Konca, H. Perfettini, L. Audin, E. J. Fielding, F. Ortega, and R. Cavagnoud (2010), Source model of the 2007 M-w 8.0 Pisco, Peru earthquake: Implications for seismogenic behavior of subduction megathrusts, *J. Geophys. Res.*, 115, B02405, doi:10.1029/2009JB006429.
- Song, T. R. A., and M. Simons (2003), Large trench-parallel gravity variations predict seismogenic behavior in subduction zones, *Science*, 301(5633), 630-633, doi:10.1126/science.1085557.
- Subarya, C., M. Chlieh, L. Prawirodirdjo, J. P. Avouac, Y. Bock, K. Sieh, A. J. Meltzner, D. H. Natawidjaja, and R. McCaffrey (2006), Plate-boundary deformation associated with the great Sumatra-Andaman earthquake, *Nature*, 440(7080), 46-51, doi:10.1038/nature04522.
- Suito, H., T. Nishimura, M. Tobita, T. Imakiire, and S. Ozawa (2011), Interplate fault slip along the Japan Trench before the occurrence of the 2011 off the Pacific coast of Tohoku Earthquake as inferred from GPS data, *Earth Planets Space*, 63(7), 615-619, doi:10.5047/eps.2011.06.053.
- Tong, X., et al. (2010), The 2010 Maule, Chile earthquake: Downdip rupture limit revealed by space geodesy, *Geophys. Res. Lett.*, 37, L24311, doi: 10.1029/2010GL045805.
- Vargas, G., M. Farias, S. Carretier, A. Tassara, S. Baize, and D. Melnick (2011), Coastal uplift and tsunami effects associated to the 2010 M(w) 8.8 Maule earthquake in Central Chile, *Andean Geology*, 38(1), 219-238.
- Victor, P., M. Sobiesiak, J. Glodny, S. N. Nielsen, and O. Oncken (2011), Long-term persistence of subduction earthquake segment boundaries: Evidence from Mejillones Peninsula, northern Chile, *J. Geophys. Res.*, 116, B02402, doi:10.1029/2010JB007771.
- Vigny, C., et al. (2011), The 2010 Mw 8.8 Maule megathrust earthquake of central Chile, monitored by GPS, *Science*, 332(6036), 1417-1421, doi:10.1126/science.1204132.
- Volker, D., I. Grevemeyer, M. Stipp, K. Wang, and J. He (2011), Thermal control of the seismogenic zone of southern central Chile, *J. Geophys. Res.*, 116, B10305, doi:10.1029/2011JB008247.
- Wells, R. E., R. J. Blakely, Y. Sugiyama, D. W. Scholl, and P. A. Dinterman (2003), Basin-centered asperities in great subduction zone earthquakes: A link between slip, subsidence, and subduction erosion?, *J. Geophys. Res.*, 108(B10), 2507, doi:10.1029/2002JB002072.
- Yagi, Y., M. Kikuchi, and T. Nishimura (2003), Co-seismic slip, post-seismic slip, and largest aftershock associated with the 1994 Sanriku-haruka-oki, Japan, earthquake, *Geophys. Res. Lett.*, 30(22), 2177, doi:10.1029/2003gl018189.